| | |
|---|---|
| Title | Impacts of anthropogenic source from the nuclear fuel reprocessing plants on global atmospheric iodine-129 cycle; A Model analysis |
| Author(s) | Kadowaki Masanao, Katata Genki, Terada Hiroaki, Suzuki Takashi, Hasegawa Hidenao, Akata Naofumi, Kakiuchi Hideki |
| Citation | Atmospheric Environment,184,p.278-291 |
| Text Version | Accepted Manuscript |
| URL | https://jopss.jaea.go.jp/search/servlet/search?5059880 |
| DOI | https://doi.org/10.1016/j.atmosenv.2018.04.044 |
| Right | © 2018. This manuscript version is made available under the CC-BY-NC-ND 4.0 license http://creativecommons.org/licenses/by-nc-nd/4.0/ |

# Impacts of anthropogenic source from the nuclear fuel reprocessing plants on global atmospheric iodine-129 cycle: a model analysis

**Masanao Kadowaki[a,*], Genki Katata[b], Hiroaki Terada[a], Takashi Suzuki[a], Hidenao Hasegawa[c], Naofumi Akata[d], Hideki Kakiuchi[c]**

[a] Japan Atomic Energy Agency, 2-4 Shirakata, Tokai, Naka-gun, Ibaraki, 319-1195, Japan,

[b] Ibaraki University, 2-1-1 Bunkyo, Mito, Ibaraki, 310-8512, Japan

[c] Institute for Environmental Sciences, 1-7 Ienomae, Obuchi, Rokkasho, Kamikita-gun, Aomori, 039-3212, Japan

[d] National Institute for Fusion Science, 322-6 Oroshi-cho, Toki, Gifu 509-5292, Japan

*Corresponding author: Kadowaki Masanao (kadowaki.masanao@jaea.go.jp)
Japan Atomic Energy Agency, 2-4 Shirakata, Tokai, Naka-gun, Ibaraki, 319-1195, Japan
TEL+81-29-282-5170
FAX+81-29-282-6760

**Key words**
Atmospheric iodine-129; Anthropogenic source; Concentration; Deposition; Seasonal change; Global atmospheric dispersion model

**ABSTRACT**

A long-lived radioactive iodine ($^{129}I$) is one of the major waste due to the human's nuclear activity. Although the behavior of $^{129}I$ in the atmosphere has been still unknown due to lack of its continuous monitoring, we recently observed clear seasonal trends in gaseous and particulate concentration and deposition of $^{129}I$ in Japan. With use of these data, we developed a global atmospheric $^{129}I$ transport model to reveal key processes for global atmospheric $^{129}I$ cycle. The physical and chemical processes of advection, turbulent diffusion, dry and wet deposition, photolysis, gas–particle conversion in the atmosphere, anthropogenic source of $^{129}I$ from nuclear fuel reprocessing plants, and volatilization from ocean and land surfaces were included into the model. The model generally reproduced the observed seasonal variation in monthly air concentration and deposition of $^{129}I$ in Japan, and the global distribution of $^{129}I$ concentration in rain from the literature. Numerical experiments with changing the intensity of anthropogenic and natural $^{129}I$ sources were carried out to quantify the impact of anthropogenic source on global $^{129}I$ cycle. The results indicated that seasonal changes in $^{129}I$ concentration and deposition at the areas far away from anthropogenic source from three nuclear fuel reprocessing plants were determined by the processes of dispersion, photolysis, and rainfall. In particular, the anthropogenic atmospheric $^{129}I$ were readily deposited during the wintertime and can be accumulated mainly in Europe and northern part of Eurasia. This result suggested that the re-emission process of $^{129}I$ from those areas may be important as secondary environmental impact of $^{129}I$ in the global scale.

## 1. Introduction

Iodine-129 ($^{129}$I), which has a long half-life of $1.57 \times 10^7$ years, has been known as a useful geochemical tracer both in marine environments and in the atmosphere (Fehn et al., 2003; Moran et al., 1995; Nimz, 1998; Michel et al., 2012). $^{129}$I is produced naturally via the interaction of atmospheric xenon with cosmic rays or the spontaneous fission of $^{238}$U and $^{235}$U in the lithosphere (Eissenbud and Gesell, 1997). The natural inventory of $^{129}$I has been estimated to be approximately 1.5 TBq (Rao and Fehn, 1999). Meanwhile, $^{129}$I is also a major radionuclide byproduct of human nuclear activities since the 1940s. Due to its long half-life and continued release from ongoing nuclear energy production, $^{129}$I is perpetually accumulating in the environment.

Anthropogenic $^{129}$I has been released into the environment due to nuclear weapons testing, nuclear accidents, and activities at nuclear fuel reprocessing plants, and is therefore distributed unevenly in the globe. Nuclear weapons testing, mainly conducted in the 1960s, dispersed $^{129}$I at 0.3–1.0 TBq into the atmosphere (Raisbeck et al., 1995; Wagner et al., 1996) with additional inputs of 40 and 8 GBq during the Chernobyl accident (Gallagher et al., 2005) and the Fukushima Dai-ichi Nuclear Power Plant disaster (Hou et al., 2013), respectively. The prior and ongoing release from nuclear fuel reprocessing plants is the most important modern contributor to the environmental inventory of $^{129}$I. The total amount of $^{129}$I released from plants at Sellafield (UK) and La Hague (France) represents more than 90% of the global emission (Aldahan et al., 2007). Michel et al. (2012) showed that the total atmospheric and marine releases, as of 2005, were 0.9 TBq and 9.0 TBq from the Sellafield plant, and 0.45 TBq and 21.8 TBq from the La Hague plant, respectively. The latest annual releases of $^{129}$I to the atmosphere were reported as 11 GBq/y from the Sellafield plant in 2015 (Sellafield Ltd, 2016) and 5.8 GBq/y from the La Hague plant in 2015 (AREVA, 2014; 2016). Reithmeier et al. (2010) estimated that the annual atmospheric release is approximately 10 GBq/y from another nuclear fuel reprocessing plant currently operating at the Mayak in Russia. Additionally, as a result of environmental releases from these plants, secondary emissions of $^{129}$I from oceans and land has also become an important source of atmospheric $^{129}$I (Persson et al., 2007; Keogh et al., 2010).

The source of airborne $^{129}$I has been a topic of interest for global $^{129}$I cycling in the atmosphere (Fig. 1), and most relevant studies have been conducted with direct measurements. In Europe, Kurpp and Aumann (1999) reported that $^{129}$I concentrations in Germany were controlled by volatilization over the North Atlantic Ocean. Gómez-Guzmán et al. (2012b) suggested that air concentrations of $^{129}$I in southern Spain were mainly affected by meridional winds. Zhang et al. (2016) reported that $^{129}$I measured in atmospheric aerosols in Denmark could be attributed to secondary emissions of $^{129}$I that had been discharged into the ocean, rather than direct gaseous release from the La Hague and Sellafield facilities. Although measurements are spatially and temporally limited compared to those made in Europe, the $^{129}$I cycle has also been investigated in North America and Asia. Toyama et al. (2012) showed that atmospheric $^{129}$I present at several sites in Japan was mainly attributable to volatilization from open oceans or and released from nuclear

fuel reprocessing plants in Japan and Europe. However, the literature is sparse in terms of studies looking at the seasonal quantitative contributions of those sources.

To investigate the behavior of atmospheric $^{129}$I, numerical models have also been utilized. Reithmeier et al. (2010) simulated the climatological deposition pattern of $^{129}$I using a box model, in which advection due to zonal wind, turbulent diffusion, dry and wet deposition, and anthropogenic and natural emissions were included. The regional transport pathway of airborne $^{129}$I has been calculated based on trajectory analysis with the Hybrid Single Particle Lagrangian Integrated Trajectory (HYSPLIT) model (Gómez-Guzmán et al., 2012b, 2017). However, these models do not include chemical forms of iodine. The behavior of atmospheric iodine is also affected by its chemical form, such as elemental iodine, organic and inorganic iodide compounds, and iodide compounds adsorbed onto particles. The concentration varies with location, season, and climate as a result of the processes of advection and diffusion, atmospheric deposition, and atmospheric chemistry (Hou et al., 2009). The organic gas of $^{129}$I is transported in the atmosphere, and then, the inorganic gas is produced from the organic gas due to atmospheric iodine photolysis. The inorganic iodine species is known to exist as particulate form (Saiz-Lopez et al., 2012a; Jabbar et al., 2013).

Lately, we reported the long-term monthly continuous measurement of gaseous and particulate $^{129}$I concentration and deposition from 2006 to 2015 at Rokkasho in northern Japan (Hasegawa et al., 2017). Both gaseous and particulate $^{129}$I concentrations showed an interesting seasonal variation as high and low during the winter and summer, respectively. This tendency is opposite from that in Canada and United States of America as observed maximum and minimum $^{129}$I concentration in rain in summer and winter, respectively (Herod et al., 2015). Although the result could be related to the transport of $^{129}$I from the European nuclear fuel reprocessing plants to the United States (Moran et al., 1999), major processes and emission sources determining global atmospheric $^{129}$I cycle is still unclear.

In this study, we aimed to reveal the impact of anthropogenic emission source on global atmospheric $^{129}$I cycle using our atmospheric dispersion model. We develop an atmospheric $^{129}$I transport model that includes physical and chemical processes of $^{129}$I with anthropogenic discharge and volatilization. We evaluate the calculation result by comparing with our monthly continuous $^{129}$I data in Japan and literature data of $^{129}$I concentration in the rain in the Northern Hemisphere. On the basis of sensitivity analyses with changing modelled anthropogenic and natural source intensity, we investigate a role of these factors in global atmospheric $^{129}$I cycle.

## 2. Model description

The newly developed atmospheric $^{129}$I transport model was designed as an offline tracer model. It requires meteorological variables to calculate the transport of $^{129}$I in the atmosphere, which are simulated by an underlying meteorological model.

### 2.1. Meteorological model

To obtain variables that drive the atmospheric iodine-129 transport model, we used the Advanced Research Weather Research and Forecasting (WRF version 3.6.1) model, which is a non-hydrostatic, fully compressible model for mesoscale meteorological predictions developed by the National Center for Atmospheric Research (Skamarock et al., 2008). The WRF has been extended with a global version (Richardson et al., 2008; Zhang et al., 2012), allowing for global forecasting and weather research. The WRF forecasts the three-dimensional meteorological fields by solving several governing equations related to atmospheric dynamics using the finite difference method with a latitude-longitude grid for horizontal coordinates and eta vertical coordinates. The horizontal domain is globally common for the WRF and the atmospheric iodine-129 transport model, in which a non-conformal grid is utilized. The WRF also has various physics options to parameterize turbulence, radiation, and grid-resolved and -unresolved cloud processes, and it can be coupled with land surface processes. The WRF simulation settings used in this study are summarized in Section 3.2.

## 2.2. Atmospheric iodine-129 transport model

To simulate global transfer of $^{129}$I in the atmosphere, we developed a global atmospheric iodine-129 transport model (GEARN-FDM) designed as an offline atmospheric dispersion model with map- and terrain-following coordinates for horizontal and vertical directions. Since the last version of GEARN-FDM was a regional model, we extended it to calculate the global-scale atmospheric dispersion process by modification of map factors and its longitudinal boundary conditions. At polar boundaries, flux and gradient calculations across the pole were not allowed because of the use of C-grid v-stagger points. However, this did not preclude advection of material across the pole, which was instead accomplished by zonal transport within the most poleward zone.

Since there are few available data of chemical compounds including $^{129}$I, we focused on two gaseous species of organic ($CH_3I$) and inorganic (I) forms and aerosol-associated particles, which have been identified as typical compounds of iodine in the atmosphere (Moran et al., 1999; Englund et al., 2010; Saiz-Lopez et al., 2012a). Thus, organic and inorganic gaseous and particulate forms of $^{129}$I were considered as airborne tracers in the model. Additionally, we modeled physical and chemical processes of $^{129}$I: 1) dry deposition, 2) wet deposition, 3) atmospheric photolysis, 4) gas–particle conversion, 5) anthropogenic release from nuclear fuel reprocessing plants, and 6) volatilization from oceans and land. The three-dimensional advection-diffusion equation of $^{129}$I for organic and inorganic gases and particle (subscripts o, i, and p, respectively) was as follows:

$$\frac{dC}{dt} = A + D + D_{Pd} + D_{Pw} + P_C + G_P + P_a + P_n, \quad (1)$$

where C is the air concentration of organic and inorganic gaseous and particulate forms of $^{129}$I, defined as $C = (C_o, C_i, C_p)$ (Bq/m$^3$); $A$ and $D$ represent advection and vertical diffusion, respectively (Kadowaki et al., 2017); $P_a$ and $P_n$ are production terms due to anthropogenic and natural emissions,

respectively; $D_{Pd}$ and $D_{Pw}$ are dry and wet deposition terms, respectively, defined as $D_{Pd} = (D_{Pdo}, D_{Pdi}, D_{Pdp})$ and $D_{Pw} = (D_{Pwo}, D_{Pwi}, D_{Pwp})$; and $P_C$ and $G_P$ are atmospheric photolysis and gas–particle conversion terms, respectively, defined as $P_C = (P_{Co}, P_{Ci}, P_{Cp})$ and $G_P = (G_{Po}, G_{Pi}, G_{Pp})$. The employed emissions for the global $^{129}$I simulation are shown in Section 3.3 and 3.4. These terms were applied to organic and inorganic gaseous and particulate forms of atmospheric $^{129}$I. The relationships between the forms of atmospheric $^{129}$I and the included processes are shown in Fig. 1.

2.2.1. Dry deposition

Dry deposition of gases and particle is represented by dry deposition velocity and the air concentration according to the inferential technique (Hicks et al., 1987) as follows:

$$D_{Pdo} = -\frac{V_{d_o} C_o}{z_1}, \quad (2)$$

$$D_{Pdi} = -\frac{V_{d_i} C_i}{z_1}, \quad (3)$$

$$D_{Pdp} = -\frac{V_{d_p} C_p}{z_1}, \quad (4)$$

where $V_{do}$, $V_{di}$, and $V_{dp}$ (m/s) are the dry deposition velocities for organic gaseous, inorganic gaseous, and particulate $^{129}$I, respectively; $z_1$ (m) is the depth of the atmospheric bottom layer, where the dry deposition process is applied. Values for dry deposition velocities for gaseous and particulate iodine were summarized by Sportisse (2007). Although the dry deposition velocity depends greatly on land use, there are few available data for the velocity over various land uses, including the sea surface. Therefore, we adopted the constants of $(V_{do}, V_{di}, V_{dp}) = (5 \times 10^{-4}, 5 \times 10^{-3}, 3 \times 10^{-2})$ as representative values for the entire simulation domain.

2.2.2. Wet deposition

Wet deposition was calculated by a simple function of scavenging coefficients (Terada et al., 2013). The decrease in the concentration by wet deposition was calculated as

$$D_{Pwo} = -\Lambda_o C_o, \quad (5)$$
$$D_{Pwi} = -\Lambda_i C_i, \quad (6)$$
$$D_{Pwp} = -\Lambda_p C_p, \quad (7)$$

where $\Lambda_o$, $\Lambda_i$, and $\Lambda_p$ (1/s) are the scavenging coefficients for organic gaseous, inorganic gaseous, and particulate $^{129}$I, respectively. In the model, two types of precipitation were considered: non-convective precipitation resolvable in the model grid scale and irresolvable convective precipitation. Using both precipitation intensities, the scavenging coefficient was calculated as

$$\Lambda = \alpha(P_{nc} + P_c)^{\beta}, (8)$$

where $P_{nc}$ and $P_c$ are the non-convective and convective precipitation intensities, respectively, which are calculated by a meteorological model; and $\alpha$ and $\beta$ are empirical constants that depend on the scavenged species and their chemical forms in the atmosphere. In this study, we adopted the typical values of $(\alpha, \beta)$ = ($8 \times 10^{-7}$, 0.6), ($8 \times 10^{-5}$, 0.6) and ($8 \times 10^{-5}$, 0.8) for organic, inorganic gas and particle, respectively (Päsler-Sauser, 2003). GEARN-FDM assumes that the scavenging by non-convective precipitation occurs in a model grid cell where the sum of the mixing ratios of rainwater, snow, and graupel is greater than zero, and the non-convective precipitation occurs at the ground below the cell. As for scavenging by convective precipitation, the model assumes that it occurs in the cell between the cloud top and the ground surface.

2.2.3 Atmospheric photolysis

Our atmospheric iodine-129 transport model included an atmospheric photolysis scheme to calculate the distribution ratio of concentration between organic and inorganic gaseous forms of $^{129}$I. The organic gas undergoes photolytic dissociation, leading to the formation of iodine atoms (Vogt, 1999):

$$CH_3I + h\nu \rightarrow CH_3 + I. (9)$$

We assumed that any produced iodine atoms would behave as inorganic compounds of iodine in the atmosphere shortly thereafter. The decrement of organic gas and the increment of inorganic gas via the photolytic reaction were calculated as

$$P_{Co} = -JC_o, (10)$$
$$P_{Ci} = JC_o, (11)$$

where $J$ (min$^{-1}$) is the photolysis rate of the reaction described by Eq. (9) for clear sky. The photolysis rate was given as a function of the solar zenith angle, $Z$ (rad) (Carter, 2007), as follows:

$$J = 1.19 \times 10^{-3} \times (\cos Z)^{0.528} \times exp(-0.833/\cos Z). (12)$$

The photolytic reaction occurs during daytime, when $Z$ is positive. Furthermore, we introduced cloud attenuation effect on the photolysis. A description of the cloud attenuation effect included in GEARN-FDM is presented in the following. Below the cloud, the photolysis rate is corrected by:

$$J_b = J[1 + f_c(1.6tr_c \cos Z - 1)], (13)$$

where $J_b$ is the photolysis rate for below cloud, $f_c$ is the cloud fraction for a grid cell, which is calculated by the meteorological model, $tr_c$ is cloud transmissivity. The above formulation leads to a lower value for the photolysis rates below the cloud, where the cloud transmissivity is reduced. Above the cloud, the photolysis rate is modified as:

$$J_a = J[1 + f_c \cos Z\,(1 - tr_c)], \quad (14)$$

where $J_a$ is the photolysis rate for above cloud. This is to allow for the photolysis rate enhancement resulting from the reflected radiation from the cloud top. Within the cloud, the photolysis rates are obtained by interpolating between cloud base and cloud top values. Therefore, on the basis of the formulation above, the cloud transmittance and cloud fraction are required for calculating cloud correction for photolysis rates. In GEARN-FDM, the calculation of cloud transmissivity is parameterized. The formulation is based on the parameterization suggested by Stephens (1978). By obtaining cloud thickness $H_c$ and liquid water content $w_c$, the liquid water path $l_{wp}$ (g/m2) is calculated as

$$l_{wp} = w_c H_c. \quad (15)$$

Then the cloud optical depth $\tau_c$ as a function of liquid water path, assuming that the drop-size distribution within the cloud column is uniform, is calculated as [Stephens, 1978]:

$$\tau_c = 10^{\left(0.2633+1.7095\ln[1og_{10}(l_{wp})]\right)}. \quad (16)$$

Finally, cloud transmissivity is calculated as:

$$tr_c = \frac{5-e^{-\tau_c}}{4+0.42\tau_c}\ . \quad (17)$$

For optically thin clouds where $\tau_c < 5$, cloud attenuation effect is not performed.

2.2.4 Gas–particle conversion

Tsukada et al. (1995) suggested that the gas–particle conversion of airborne iodine is dependent on atmospheric temperature. Fig. 2 shows a scatter plot of atmospheric temperature and the gas–particle ratio to the total concentration factor of $\zeta$, which was defined as $\zeta = C_p/(C_p + C_i)$. These data were measured in Chiba, Japan, from June 1991 to February 1992 (Tsukada et al., 1995). Based on these measurements, we approximated the relationship between atmospheric temperature and $\zeta$ using the least squares method with a linear function,

$$\zeta = -0.0191(T - 273.15) + 0.886, \quad (18)$$

where $\zeta$ ranges between 0 and 1 and $T$ (K) is atmospheric temperature. We assumed that inorganic gas and particles of iodine were under concentration equilibrium at any location. By using the factor from Eq. (18), the concentration of inorganic gaseous and particulate $^{129}$I in equilibrium were calculated as

$$C_i^{eq} = (1-\zeta)\left(C_p + C_i\right), \quad (19)$$

$$C_p^{eq} = \zeta\left(C_p + C_i\right), \quad (20)$$

where $C_i^{eq}$ and $C_p^{eq}$ denote the inorganic gaseous and particulate concentration in equilibrium. Thus, the concentration fluctuation due to the gas–particle conversion was calculated as

$$G_{Pi} = \frac{C_i^{eq} - C_i}{\tau}, \quad (21)$$

$$G_{Pp} = \frac{C_p^{eq} - C_p}{\tau}, \quad (22)$$

where $\tau$ (s) is the relaxation time for gas–particle partitioning to reach the concentration in equilibrium. As suggested by previous experimental data, into the iodine gas–particle conversion process, the relaxation time was set to 14 days (Uematsu et al., 1988).

## 3. Data for model validation and simulation settings

### 3.1 Measurement data

We evaluated our model to reproduce our latest data of monthly gaseous and particulate air concentration and (total) deposition of $^{129}$I measured at the Institute for Environmental Sciences in Rokkasho, Japan (40°57 N, 141°21E) from 2009 to 2010 (Fig. 3). The procedure for measuring air concentration are given here. An aerosol filter paper (QR-100, Toyo Roshi Kaisha, Ltd., Japan), an activated charcoal-impregnated filter paper (CP-20, Toyo Roshi Kaisha, Ltd., Japan) and an activated charcoal cartridge (CHC-50, Toyo Roshi Kaisha, Ltd., Japan) were used in series for collecting samples of particulate and gaseous iodine in the atmosphere. The CP-20 and CHC-50 media were impregnated with a 10 wt.% solution of triethylenediamine to improve its collecting performance, especially for less reactive iodine compounds, such as methyl iodine. Air was introduced into a sampling unit at a flow rate of 30 L/min through the QR-100 filter. The sampling unit contained the CP-20 filter and three CHC-50 cartridges in series. After sampling for one month, iodine was extracted from the samples in accordance with the methods of Lopez-Gutierrez et al. (1999), and gaseous and particulate $^{129}$I concentration were measured by accelerator mass spectrometry (with an upgraded HVEC model FN-8MV) at the PRIME Laboratory (Purdue University). Details in the sampling and analysis methods for the deposition samples were described in Hasegawa et al. (2017).

Although the sampling periods are unavoidably different among the datasets, we additionally used for available data of $^{129}I$ concentration in rain in the literature to evaluate modelled spatial distribution of global atmospheric $^{129}I$ cycle.

### 3.2. Physical schemes in models

The settings for the WRF and GEARN-FDM are summarized in Table 1. Meteorological variables were calculated by the WRF, which incorporated several physical and dynamic processes. In this study, the Mellor-Yamada-Nakanishi-Niino (MYNN2.5) model (Nakanishi and Niino, 2004) was used for planetary layer turbulence calculations which were used to derive the turbulent diffusivity of airborne $^{129}I$. The six-class scheme WSM6 (Lin et al., 1983) was selected for the grid-scale cloud microphysics model. Sub-grid-scale cumulus convection was parameterized using the new simplified Arakawa-Schubert scheme (Han and Pan, 2011). Atmospheric radiative transfer was solved using the Rapid Radiative Transfer Model (RRTM) (Mlawer et al., 1997) for longwave radiation and the Dudhia scheme (Dudhia, 1989) for shortwave radiation. The Noah LSM (Land Surface Model) was used (Chen and Dudhia, 2001) to calculate the land surface heat and moisture exchange.

### 3.3. Anthropogenic source of Iodine-129

Although $^{129}I$ has produced and released into the atmosphere by prior nuclear weapons testing and nuclear accidents, nuclear fuel reprocessing plants are by far the largest contributors to the current release of $^{129}I$ (Snyder et al., 2010). The La Hague, Sellafield, and Mayak facilities are well-known operating plants. Fig. 4 shows the annual radioactivity of $^{129}I$ released from nuclear fuel reprocessing plants during the simulation period. Although there are available data for the amount of atmospheric $^{129}I$ released from La Hague and Sellafield, such data for Mayak has not been disclosed. Therefore, we used the 10 GBq/y estimate from Reithmeier et al. (2010) for atmospheric $^{129}I$ released from Mayak. The released mass does not vary hourly or daily in the simulation, but it fluctuates annually, as shown in Fig. 4. The release flux of $^{129}I$ from each plant was calculated by dividing the annual release radioactivity by the area of the grid where the plant is located and the period of 365 days (366 days for 2008).

The United Nations Scientific Committee on the Effects of Atomic Radiation (UNSCEAR) reported that measurements from the Sellafield plant indicate that 60% of the iodine in the off-gases is in organic form, 40% in inorganic form, and less than 1% in particulate form (Moran et al. 1995; IAEA, 2014). Therefore, we assumed that 60% of the total amount of $^{129}I$ released from the Sellafield was organic and 40% was inorganic gases. Since there is no available data for the fraction of the La Hague and Mayak, we further assumed that these two plants had the same off-gas composition as Sellafield.

### 3.4. Natural source of Iodine-129

The short residence time of iodine in the atmosphere (organic gas: 18 days; inorganic gas: 10 days; particles: 14 days) suggests that most of the iodine released into the atmosphere is returned to Earth's surface shortly thereafter (Rahn et al., 1976). Therefore, volatilization from the shallow ocean and land is an important source for airborne iodine.

Since there are few measurements from which to calculate the volatilization flux of $^{129}I$ from the ocean, we calculated it by multiplying the global sea-to-air flux of stable iodine ($^{127}I$) by the ratio of $^{129}I/^{127}I$ in the shallow ocean (Snyder et al., 2010). In this study, we assumed that the volatile form of $^{129}I$ was organic gas ($CH_3I$). Ziska et al. (2013) calculated the global sea-to-air flux climatology of organic gaseous $^{127}I$ based on surface oceanic and atmospheric measurements. According to their approach, we calculated the flux climatology, where daily sea surface temperatures, horizontal winds, and surface pressures within ERA-interim reanalysis were used as input variables. The $^{129}I/^{127}I$ ratio in the ocean was summarized by Snyder et al. (2010). Since the spatial distribution of the ratio is limited, we divided the oceans into eight areas: the Arctic Ocean, northern and southern areas of the North Atlantic Ocean, the South Atlantic Ocean, the North Pacific Ocean, the South Pacific Ocean, the Indian Ocean, and the Antarctic Ocean. Based on this division, we calculated area-averaged values of $^{129}I/^{127}I$ the ratio for each area (Table 2). Since there are few available data for the ratio in oceans in the Southern Hemisphere except for the Indian Ocean, we used $5.0 \times 10^{-11}$, from the above-ground Nuclear testing level for the ratio of the South Atlantic Ocean and the South Pacific Ocean. In addition to these oceans, we used $1.5 \times 10^{-12}$, the pre-anthropogenic level, for the ratio of the Antarctic Ocean. In addition to oceanic emissions, the volatilization of $^{129}I$ from land was included in the model, and 2.6 GBq/y was used for the global volatilization flux (Snyder et al., 2010). The flux of $^{129}I$ from land is globally uniform.

### 3.5. Simulation scenarios

The initial atmospheric concentration of organic and inorganic gaseous and particulate forms of $^{129}I$ in the simulation domain were set to zero. The simulation period lasted five years, from January 1, 2006, to January 1, 2011. The simulated results for the first three years, from 2006 to 2008, were excluded because the cutting and chemical processing of nuclear fuel was tested at a nuclear fuel reprocessing plant which is located 2 km west of the measurement site (Hasegawa et al., 2017) from April 2006 to April 2008.

As shown in Table 2, several simulation scenarios using GEARN-FDM were carried out to investigate the impacts of atmospheric physical and chemical processes and anthropogenic source of $^{129}I$ on global atmospheric $^{129}I$ cycle. In the NRP (**N**uclear fuel **R**eprocessing **P**lants: $^{129}I$ emission from nuclear fuel reprocessing plants) simulation, the only anthropogenic source is considered by setting both values of $^{129}I$ volatilization fluxes from the ocean and land to zero. On the other hand, in the NAT (**N**orth **AT**lantic Ocean: $^{129}I$ emission from the North Atlantic Ocean) and NPF (**N**orth **P**aci**F**ic Ocean: $^{129}I$ emission from the North Pacific Ocean) simulations, we set the flux of $^{129}I$ other than from the North Atlantic Ocean and the North Pacific Ocean, respectively, to zero. For the LAND ($^{129}I$ emission from land surface) simulation, we set the anthropogenic release from the

nuclear fuel reprocessing plants and $^{129}$I volatilization fluxes of ocean, respectively, to zero. To quantify the impact of modeled gas–particle conversion processes, an additional simulation of the RT1D (**R**elaxation **T**ime of **1 D**ay: 1 day of the relaxation time) with very short relaxation time of 1 day for $\tau$ in Eqs. (21) and (22) was conducted.

## 4. Results and discussion

### 4.1. Model validation

#### 4.1.1. Seasonal changes in iodine-129 concentration and deposition in Japan

Before validating the simulation result, we preliminary show the global distribution of simulated $^{129}$I concentrations and deposition. Fig. 5 illustrates the horizontal distribution of seasonally averaged surface air concentration of total gaseous $^{129}$I and accumulated total deposition of $^{129}$I in the Control simulation. In winter, the simulated concentration was more than 0.5 nBq/m$^3$ in the Northern Hemisphere, with relatively high concentrations appearing zonally at mid- and high-latitudes due to tropospheric zonal jet (Fig. 5a). The deposition globally occurred in the Northern Hemisphere except for specific area, in which rainfall was very small (Fig. 5c). On the other hand, the simulated concentration in summer was globally lower than those predicted in winter (Fig. 5b). The horizontal distribution of the concentration in the mid- and high-latitudes in summer was mainly attributed by seasonal wind pattern (not shown in Fig. 5) and wet deposition in summertime (Fig, 5d).

To validate the performance of our model, we compared the results of the Control simulation with the empirical measurements. Fig. 6 shows the comparison between the simulation and the measurements for surface air concentration of gaseous and particulate $^{129}$I, $^{129}$I concentration in rain, and monthly rainfall at Rokkasho in the Control simulation. The gaseous concentration (Fig. 6a) is a sum of the simulated organic and inorganic gaseous $^{129}$I concentration. Table 3 presents the results of a statistical analysis of the simulation and measurement results at Rokkasho, showing the mean, minimum and maximum, median, and standard deviation (SD) of the simulation and measurement results. It also includes the results of a statistical comparison of the two sets of results, including the mean bias (MB), root mean square error (RMSE), correlation coefficient (R), ratio of simulated-to-measured medians (RSMM) and the fraction of data within factors of 2 (FA2).

The simulated gaseous $^{129}$I concentration showed month-to-month variability, with relatively high and low concentration appearing in winter and summer, respectively (Fig. 6a). The organic gas concentration was approximately two orders of magnitudes higher than the inorganic concentration (not shown in Fig. 6a), indicating the organic gas was the significant compound of total gaseous $^{129}$I concentration. Similar variations were evident in the measurements: the simulated and measured gaseous concentration had a reasonably positive correlation (R = 0.56), and the actual concentration values were quantitatively well-matched (RSMM = 0.83 and FA2 = 0.63). The seasonal variation was also clearly shown in the simulated particulate $^{129}$I concentration, in which the relatively high and low concentration appeared in winter and summer, respectively (Fig. 6b).

Although the simulated particulate concentration values were slightly underestimated, their seasonal variation was similar to that of the measured data (R = 0.36, RSMM = 0.59 and MB = −0.42). The volatilization of inorganic forms of $^{129}$I from ocean does not included in GEARN-FDM. If the inorganic $^{129}$I emission is employed in the model, the simulated inorganic gaseous $^{129}$I concentration may become higher, furthermore, resulting in increasing the particulate $^{129}$I concentration throughout the gas-particle conversion process. In addition to the volatilization of inorganic forms of $^{129}$I, sea spray may contribute directly to the particulate $^{129}$I concentration. In localities proximal to coastal areas, the sea spray may be a major contributor of iodine to the land (Fuge and Johnson, 2015). Furthermore, the underestimation may be attributed by the used relaxation time. The uncertainty of the relaxation time is discussed in Section 4.1.3.

Although the simulated $^{129}$I concentration in rain underestimated the measured values (MB = −0.83 and RSMM = 0.18), the seasonal variation was in agreement between calculations and observations with a high correlation as shown in Fig. 6c (R = 0.62). The temporal variation of the simulated and measured monthly accumulated rainfall at Rokkasho, and results of the statistical analysis for the rain, are shown in Fig. 6c and Table 3, respectively. The seasonal variations of the simulated and measured rain were in good agreement (R = 0.84, RSMM = 0.87 and FA2 = 0.96). The simulated $^{129}$I concentration in rain showed clear seasonal variation ranging from 0.02–0.33 μBq/L with the mean and median values of 0.10 and 0.08 μBq/L in the simulation, respectively. During the same period, the measured concentration showed seasonal variation similar to the model, ranging between 0.10 and 5.57 μBq/L, and the mean and median were 0.93 μBq/L and 0.45 μBq/L, respectively (Table 3).

4.1.2. Global distribution of iodine-129 concentration in rain

In addition to the comparison at Rokkasho, we compared the simulation results with measured values in locations around the globe in order to evaluate the global distribution of simulated $^{129}$I. Fig. 7 shows the comparison of simulated and measured $^{129}$I concentration in rain in Europe, Asia, and North America (the locations are shown in Fig. 3). The period of measurements shown in Fig. 7 and Table 4 are different from that of the simulation, but we compare the simulated $^{129}$I concentration with measured one using a statistical method in order to validate the spatial distribution of simulated concentration.

In Europe, the simulated concentration in Nordic countries showed a range of $10^{8}$–$10^{10}$ atmos/L, which agreed well with measured values except for Bergen (Persson et al., 2007; Xu et al., 2013). The underestimation in Bergen resulted from our access to only two measurements, which introduces considerable uncertainty. The simulated concentration at Abisko and Uppsala were lower than those in Kividinge and Roskilde, mirroring the empirical tendencies. Additionally, the mean and median values produced by the simulation were close to the measured values. The simulated concentration in Bavaria were similar to the measurements, with comparable mean and median values (Reithmeier et al., 2005). The simulated concentration in Seville were 1–2 orders of magnitude lower than those in the Nordic countries and in Bavaria, and mostly ranged between $10^{7}$

458 and $10^8$ atmos/L, which agrees well with observations (López-Gutiérrez et al., 2001; 2004; Gómez-
459 Guzmán et al., 2012b). Furthermore, the contrast of the measured concentration between northern
460 and southern parts of Europe was clearly observed in the simulation results.
461 In Asia, the simulated concentration was approximately an order of magnitude lower than
462 those in Europe, matching the measurements. At Fukushima and Tsukuba, when ignoring outliers,
463 the ranges of simulated concentrations fell within the measured range, and the values of mean and
464 median for the simulated concentration were in reasonably good agreement with the measurement
465 metrics (Xu et al., 2013; Toyama et al., 2013). Additionally, at Ishigaki island, the range, mean, and
466 median of the simulated concentration were mostly the same as those of the measured ones
467 (Toyama et al., 2013).
468 In North America, the simulated concentration levels were similar of those in Asia, which
469 matched the measurements. At the sites of Vancouver, Saturna, and NADP-WA19, the range, mean,
470 and median values of the simulated concentration were approximately the same as those of the
471 measured ones (Herod et al., 2015). Based on these comparison results, the simulation has
472 demonstrated an ability to reasonably model the spatial distribution of atmospheric $^{129}$I in the
473 Northern Hemisphere.
474
475 4.1.3 Uncertainty of gas–particle conversion modeling
476 The impact of modelled gas–particle conversion on the simulation result was evaluated by
477 a sensitivity test named as RT1D (very short relaxation time of gas-particle conversion).
478 Figure 8 shows the temporal variations of monthly gaseous and particulate $^{129}$I
479 concentrations at Rokkasho in the RT1D and Control scenarios. For total gas, the results of the
480 RT1D model were similar to those of the Control (Fig. 8a). However, the inorganic gaseous
481 concentrations in the RT1D simulation were lower than the Control. By contrast, the particulate
482 concentration that appeared in the RT1D simulation was approximately five times higher than that
483 in the Control (Fig. 8b), evidence that the inorganic gaseous and particulate $^{129}$I concentrations were
484 significantly affected by the relaxation time for the gas–particle conversion process. When the
485 relaxation time was longer, air concentration of particulate and inorganic gas increased and
486 decreased, respectively. The introduced relaxation time was estimated by gaseous and particulate
487 concentrations of airborne iodine measured over the North Pacific Ocean between May 6–14, 1988
488 (Uematsu et al., 1988). The total deposition in the RT1D simulation was still an underestimation of
489 the measured values (Fig. 8c). As mentioned in Section 4.1.1, no emission of inorganic and
490 particulate forms of 129I from ocean may result in this underestimation. Furthermore, this
491 underestimation may be resulted from the wet deposition process. The deposition of airborne 129I
492 occurs not only by the precipitation but also by fog-water, and the deposition velocities of gaseous
493 and particulate 129I of fog-water deposition is 1–4 orders of magnitude larger than that of dry
494 deposition (Katata et al., 2015). Although the lack of available data makes it difficult to validate the
495 accuracy of the modeled structure, the vertical structure of airborne 129I also contributes to the total
496 deposition.

4.2. Impacts of anthropogenic source on global iodine-129 cycle

In order to clarify the influence of anthropogenic source on global $^{129}$I cycle in the atmosphere, we carried out numerical experiments to investigate the contributions of all emission sources (Fig. A1) to the air concentration and deposition of $^{129}$I in Japan (Rokkasho) and Canada (Vancouver) which were located far away from anthropogenic release points (Fig. 5, Nos. 1–3).

Figure 9 shows the temporal changes in monthly surface air concentration of gaseous and particulate $^{129}$I, total deposition of $^{129}$I, and rainfall calculated in the Control simulation. At both sites, a large part of the air concentration of $^{129}$I was occupied by organic gas (Figs. 9a and 9b). Since organic gas was not removed very rapidly along the way of its transport by wet deposition due to very low scavenging coefficient (Eq. 8), the temporal change of air concentration of $^{129}$I could be explained mainly by advection, diffusion and decomposition due to photolysis.

Comparing with the time series of total gaseous $^{129}$I concentration, those of total deposition at both sites were slightly different (Fig. 9c). The maximum peak of deposition in Japan on March 2010 synchronized with that of inorganic gas concentration (Fig. 9b), suggesting that inorganic gas dominantly affects the total deposition because the scavenging coefficient of inorganic gaseous $^{129}$I is larger than that of organic one (Eq. 8). In Canada, the seasonal change in total deposition has relatively unclear as that of inorganic gas concentration, while relatively low values in July 2009 and 2010 would be influenced by low values in both organic gas concentration and rainfall amount (Figs. 9a and d). Therefore, both gas concentration and rainfall amount were important to determine total deposition at the places far away from anthropogenic sources.

Figure 10 shows the contribution of each source to surface air concentration and deposition of $^{129}$I in Japan and Canada from 2009 to 2010 in different simulation scenarios. In winter, the (mainly organic) gaseous concentration was high (Fig. 9a) and the anthropogenic source from three nuclear fuel reprocessing plants contributed to 36 and 30% of all sources in Japan and Canada, respectively (Figs. 10a and 10b). The rest was primarily originated from natural emissions from the North Pacific Ocean and land surfaces. Similar levels of the impact of anthropogenic sources on total deposition were found as 37–45% and 30–40% in Japan and Canada, respectively. Meanwhile, in summer, anthropogenic sources has less contribution of both concentration and deposition of $^{129}$I gases (Fig. 10c). The result indicates that, during the wintertime, the anthropogenic $^{129}$I tends to disperse and deposit due to long-range transport in the semi-global scale.

Figure 11 illustrates the horizontal distributions of seasonally averaged surface air concentration of total gas and deposition of $^{129}$I and rainfall in the NRP ($^{129}$I emission from only European nuclear fuel reprocessing plants) scenario. Compared with the summertime, the high concentration areas were relatively uniformly distributed during the wintertime (Figs. 11a and 11b) in the surrounding area of anthropogenic sources due to seasonal westerly wind in mid-latitude atmosphere over the Northern Hemisphere (not shown in figure). In contrast, high deposition areas during the wintertime was limited to the land of Europe and norther part of Eurasia with high

rainfall (Fig. 11e). This suggests that anthropogenic $^{129}$I tends to be deposited onto these areas every winter period.

An important hypothesis that long-term accumulation (deposition) of anthropogenic $^{129}$I over the land of Europe and norther part of Eurasia becomes aerial sources would be raised from a large amount of total deposition calculated in these areas in summer (Fig. 11d). Although the anthropogenic source has directly low impact on deposition at the sites far away from the source (Fig. 10), as depicted in Fig. 1, organic $^{129}$I gas accumulated in these areas can volatilize via the vegetative surface (Amiro and Johnston, 1989). Since total deposition originated from natural emission from the land was relatively high in Japan (Fig. 10c), such re-emission process of $^{129}$I from the areas may be important as secondary environmental impact of $^{129}$I in the global scale.

## 5. Conclusions

This study aimed to investigate the impacts of anthropogenic sources from the nuclear fuel reprocessing plants in the Northern Hemisphere on global atmospheric $^{129}$I cycle. To achieve this, we developed an atmospheric $^{129}$I transport model which includes physical and chemical processes of $^{129}$I in the atmosphere. We ran the model to reproduce the temporal variation in atmospheric gaseous and particulate $^{129}$I concentration and deposition at Japan and the global distribution of $^{129}$I concentration in rain from the literature. The simulated concentration and deposition in Europe, Asia, and North America generally agreed with observed ones, while total deposition was slightly underestimated in Asia.

Numerical experiments of the model were carried out to evaluate the influence of anthropogenic source to surface air concentration and total deposition of $^{129}$I. The seasonal variation in $^{129}$I concentration in the areas far away from anthropogenic sources was determined by the processes of advection, diffusion, and decomposition of organic gaseous $^{129}$I due to photolysis, while, the temporal change in $^{129}$I deposition was mainly determined by both concentration of $^{129}$I gas species and rainfall amount. In winter, (mainly organic) gaseous $^{129}$I concentration in Japan and Canada was high and the anthropogenic source from three nuclear fuel reprocessing plants explained 30–40 % of all emission sources for total deposition. The result also indicates that the anthropogenic $^{129}$I tended to be deposited (accumulated) over the land of Europe and norther part of Eurasia during the wintertime, suggesting that the re-emission process of the organic $^{129}$I gas from the areas would be important as secondary environmental impact of anthropogenic $^{129}$I.

## Appendix A: Estimation of $^{129}$I volatilization flux from the ocean

Fig. A1 shows the temporal variations of monthly volatilization fluxes of $^{129}$I from ocean calculated in our model. During 2009–2010 (the simulation period), the calculated flux from the all oceans was 4.9 GBq/y. This flux underestimated the former estimated volatilization flux of $^{129}$I (Snyder et al., 2010). This underestimation may be due to not considering gaseous and particulate emissions from ocean other than methyl iodide. However, the calculated flux reasonably agreed with 4–26 GBq/y of the volatilization flux estimated by using $3400 \times 10^{-12}$ of a present marine

574 $^{129}I/^{127}I$ ratio (Snyder et al., 2010) and the volatilization flux of $^{127}I$ ranging between 180 and 1162
575 Gg/y (Tegtmeier et al., 2013 and therein). Additionally, Reithmeier et al. (2006) estimated that the
576 volatilization flux of $^{129}I$ from ocean of 2004 was about 10–11 GBq/y. Assuming that the
577 volatilization flux of $^{129}I$ from ocean of 2009–2010 is as same level as that of 2004, the calculated
578 volatilization flux was comparable with the estimation volatilization flux of $^{129}I$ from ocean. The
579 calculated volatilization flux of $^{129}I$ from the North Atlantic Ocean clearly showed the seasonal
580 variations—high in winter and low in summer (Fig. A1, solid blue line). The annual amount of the
581 volatilization flux during 2009–2010 was 2.3 GBq/y, and the volatilization flux of $^{129}I$ from the
582 northern area of North Atlantic Ocean was dominant. The similar variation was found in the
583 volatilization flux of $^{129}I$ from the North Pacific Ocean (Fig. A1, red line), and the annual amount
584 was 0.74 GBq/y. The volatilization flux of $^{129}I$ from oceans in the Southern Hemisphere including
585 the Indian Ocean was lower than that calculated by the North Atlantic Ocean and the North Pacific
586 Ocean. Those volatilization fluxes except for the Antarctic Ocean were high in summer and low in
587 winter.
588
589 **Acknowledgments**
590 The authors wish to thank Dr. Mizuo Kajino of the Meteorological Research Institute of
591 Japan for useful comments and discussions. ERA-Interim reanalysis data were obtained from
592 ECMWF website (http://apps.ecmwf.int/datasets/).
593
594 **References**
595 Aldahan, A., Alfimov, V., Possnert, G., 2007. $^{129}I$ anthropogenic budget: major sources and sinks,
596 Appl. Geochem. 22, 606–618.
597 Amiro, B.D., and Jonston, F.L., 1989. Volatilization of iodine from vegetation, Atmos. Environ.
598 23(3), 533–538, doi.org/10.1016/0004-6981(89)90002-4.
599 AREVA, 2014. Rapport annuel de surveillance de l'environnement du site AREVA La Hague (only
600 in French). http://www.new.areva.com/activities/liblocal/docs/BG aval/Recyclage/La
601 hague/2015/ Rapport-environnement-LH-2014.pdf (Accessed 18 October 2017).
602 AREVA, 2016. Gaseous Release: Annual Statement. http://www.areva.com/EN/operations-
603 2332/gaseous-releases-annual-statement.html/ (Accessed 28 September 2017).
604 Carter, W. P. L., 2007. Investigation of the Atmospheric Ozone Impacts of Methyl Iodide, Center
605 for Environ. Res. and Technol. UC Riverside, 1–40.
606 Chen, F., and Dudhia, J., 2001. Coupling an advanced land‐surface hydrology model with the
607 Penn State/NCAR MM5 modeling system. Part I: Model description and implementation, Mon.
608 Weather Rev. 129, 569–585, doi:10.1175/1520-0493(2001)129<0569:CAALSH>2.0.CO;2.
609 Dudhia, J. (1989), Numerical study of convection observed during the winter monsoon experiment
610 using a mesoscale two‐dimensional model, J. Atmos. Sci. 46, 3077–3107, doi:10.1175/1520-
611 0469(1989)046<3077: NSOCOD>2.0.CO;2.

Edmonds, H. N., Smith, J.N., Livingston, H.D., Kilius, L.R., and Edmond., J.M., 1998. 129I in archived seawater samples, Deep Sea Res. Part I, 45, 1111–1125.

Eissenbud, M., Gesell, T., 1997. Environmental Radioactivity. Academic Press, San Diego.

Englund, E., Aldahan, A., Hou, X.L., Possnert, G., Söderström, C., 2010. Iodine ($^{129}$I and $^{127}$I) in aerosols from northern Europe, Nucl. Instrum. Methods Phys. Res. B 268, 1139–1141.

Fehn, U., Snyder, G.T., Matsumoto, R., Muramatsu, Y., Tomaru, H., 2003. Iodine dating of pore waters associated with gas hydrates in the Nankai area, Japan, Geology 31, 521–524.

Fuge, R., Johnson, C.C., 2015. Iodine and human health, the role of environmental geochemistry and diet, a review, Appl. Gheochem. 63, 282–302, doi.org/10.1016/j.apgeochem.2015.09.013.

Gallagher, D., McGee, E., Mitchell, P.I., Alfimov, V., Aldahan, A., Possnert, G., 2005. Retrospective search of evidence of the 1957 Windscale fire in NE Ireland using $^{129}$I and other long-lived nuclides, Environ. Sci. Technol. 39, 2927–2935.

Gómez‐Guzmán, J.M., Enamorado‐Báez, S.M., Pinto-Gómez, A.R., Abril‐Hernández, J.M., López‐Gutiérrez, J.M., García-León, M., 2012b. Anthropogenic $^{129}$I concentration and 129I/127I ratio in rainwater from Seville (Spain) in the period 2005–2008 as affected by airborne releases from Sellafield and La Hague facilities, Atmos. Environ. 56, 26–32.

Gómez‐Guzmán, J.M., López-Gutiérrez, J.M., García‐Tenorio, R., Agulló, L., Peruchena, J.I., Manjón, G., and García‐León., M., 2017. Estimating the impact from Fukushima in Southern Spain by $^{131}$I and Accelerator Mass Spectrometry detection of $^{129}$I, J. Environ. Radioact. 166, 33–44.

Han, J., and Pan, H., 2011. Revision of Convection and Vertical Diffusion Schemes in the NCEP Global Forecast System, Wea. Forecasting 26, 520–533.

Hasegawa H., Kikuchi, H., Akata, N., Ohtsuka, Y., Hisamatsu, S., 2017. Regional and global contributions of anthropogenic iodine-129 in monthly deposition samples collected in North East Japan between 2006 and 2015, J. Environ. Radioact. 171, 63–73.

Herod, M.N., Suchy, M., Cornett, R.J., Kieser, W.E., Clark, Ian D., and Graham, G., 2015. The atmospheric transport of iodine-129 from Fukushima to British Columbia, Canada and its deposition and transport into groundwater, Water Resources Res. 51, 9628–9645, doi:10.1002/2015WR017325.

Hicks, B. B., Baldocchi, D.D., Meyers, T.P., Hosker, R.P. and Matt, D.R., 1987. A preliminary multiple resistance routine for deriving dry deposition velocities from measured quantities, Water Air Soil Poll. 36, 311–330, doi:10.1007/BF00229675.

Hou, X., Aldahan, A., Nielsen, S.P., Possnert, G., Nies, H., and Hedfors, J., 2007. Speciation of $^{129}$I and $^{127}$I in seawater and implications for sources and transport pathways in the North Sea, Environ. Sci. Technol. 41, 5993–5999.

Hou, X., Hansen, V., Aldahan, A., Possnert, G., Lind, O.C. and Lujaniene, G., 2009. A review on speciation of iodine-129 in the environmental and biological samples, Anal. Chim. Acta 632, 181–196, doi:10.1016/j.aca.2008.11.013.

Hou, X.L., 2004. Application of 129I as an environmental tracer, J. Radioanal. Nucl. Chem. 262, 67–75, doi:10.1023/B:JRNC.0000040855.91732.9f.

Hou, X.L., Provinec, P.P., Zhang, L.Y., Shi, K., Biddulph, D.L., Chang, C.C., Fan, Y.K., Golser, R., Hou, Y.C., Jeskovsky, M., Jull, A.J.T., Liu, Q., Luo, M.Y., Steier, W., Zhou, W.J., 2013. Iodine-129 in sea water offshore Fukushima: distribution, inorganic speciation, sources, and budget, Environ. Sci. Technol. 47, 3091–3098.

IAEA, 2014. IAEA TECDOC SERIES, Treatment of Radioactive Gaseous Waste

Jabbar, T., Wallner, G., Steier, P., 2013. A review on $^{129}$I analysis in air, J. Environ. Radioact. 126, 45–54.

Kadowaki, M., Katata, G., Terada, H. and Nagai, H., 2017. Development of the Eulerian atmospheric transport model GEARN-FDM: Validation against the European tracer experiment, Atmos. Pollut. Res. 8, 394–402, doi.org/10.1016/j.apr.2016.10.012.

Keogh, S.M., Aldahan, A., Possnert, G., León Vintró, L., Mitchell, P.I., Smith, K.J., McGinnity, P., 2010. Anthropogenic $^{129}$I in precipitation and surface waters in Ireland, Nucl. Instrum. Methods Phys. Res. B 268, 1232–1235.

Krupp, G., and Aumann, D.C, 1999. Iodine-129 in rainfall over Germany, J. Environ. Radioact. 46, 287–299, doi:10.1016/S0265-931X(98)00148-9.

Lin, Y.‐L., Farley, R.D., and Orville, H.D., 1983. Bulk parameterization of the snow field in a cloud model, J. Clim. Appl. Meteorol. 22, 1065–1092, doi:10.1175/1520-0450(1983)022<1065:BPOTSF>2.0.CO;2.

López‐Gutiérrez, J. M., García‐León, M., Schnabel, C., Schmidt, A., Michel., R., Synal, H.-A., Suter, M, 1999. Determination of 129I in atmospheric samples by accelerator mass spectrometry. Appl. Radiat. and Isot. 51, 315–322.

López‐Gutiérrez, J. M., García‐León, M., Schnabel, C., Suter, M., Synal, H.‐A., Szidat, S., 2001. Wet and dry deposition of 129Iin Seville (Spain) measured by accelerator mass spectrometry, J. Environ. Radioact. 55, 269–282.

López‐Gutiérrez, J. M., Santos, F.J., García‐León, M., Schnabel, C., Synal, H.‐A., Ernst, T., and Szidat, S., 2004. Levels and temporal variability of $^{129}$I concentrations and 129I/127I isotopic ratios in atmospheric samples from southern Spain, Nucl. Instrum. Methods Phys. Res., Sect. B, 223–224, 493–500.

Michel, R., Daraoui, A., Gorny, M., Jakob, D., Sachse, R., Tosch, L., Nies, H., Goroncy, I., Herrmann, J., Synal, H.A., Stocker, M., Alfimov, V., 2012. Iodine-129 and iodine-127 in European seawaters and in precipitation from Northern Germany, Sci.Total Environ. 419, 151–169.

Mlawer, E. J., Taubman, S.J., Brown, P.D., Iacono, M.J. and Clough, S.A., 1997. Radiative transfer for inhomogeneous atmosphere, RRTM, a validated correlated‐k model for the long wave, J. Geophys. Res. 102, 16,663–16,682, doi:10.1029/97JD00237.

687 Moran, J. E., Oktay, S., Santschi, P.H. and Schink, D.R., 1999. Atmospheric dispersal of $^{129}$Iodine
688 from nuclear fuel reprocessing facilities, Environ. Sci. Technol. 33, 2536–2542,
689 doi:10.1021/es9900050.
690 Moran, J.E., Fehn, U., Hanor, J.S., 1995. Determination of source ages and migration patterns of
691 brines from the U.S. Gulf Coast basin using $^{129}$I, Geochim. Cosmochim. Acta 59, 5055–5069.
692 Nakanishi, M. and Niino, H., 1996. An improved Mellor–Yamada level-3 model with condensation
693 physics: Its design and verification, Mon. Wea. Rev. 124, 2046–2070
694 Nies, H., et al., 2009. Kartierung von Tc‐99, I‐129 und I‐129 im Oberflächenwasser der
695 Nordsee, Vorhaben StSch 4481, 204, Bundesamt für Strahlenschutz, Salzgitter, Germany.
696 Nimz, J.G, Kendall, C., McDonnell, J., 1998. (Eds.), Lithogenic and Cosmogenic Tracers in
697 Catchment Hydrology; Isotope Tracers in Catchment Hydrology, first ed. Elsevier.
698 Päsler‐Sauer, J., 2003. Description of the atmospheric dispersion model ATSTEP. Version
699 RODOS PV 5.0. Technical Report RODOS(RA2)-TN(03)-01, Forschungszentrum Karlsruhe
700 GMBH.
701 Persson, S., Aldahan, A., Possnert, G., Alfimov, V., Hou, X., 2007. $^{129}$I Variability in precipitation
702 over Europe, Nucl. Instrum. Methods Phys. Res. B 259, 508–521.
703 Rahn K.A., Borys, R.D. and Duce, R.A., 1976. Tropospheric halogen gases: inorganic and organic
704 components, Science 192, 549-550.
705 Raisbeck, G.M., Yiou, F., Zhou, Z.Q., Kilius, L.R., 1995. $^{129}$I from nuclear reprocessing facilities at
706 Sellafield (UK) and La Hauge (France): potential as an oceanographic tracer, J. Mar. Syst. 6,
707 561–570.
708 Rao, U. and Fehn, U., 1999. Source and reservoirs of anthropogenic Iodine-129 in western New
709 York. Geochimica Cosmochimica Acta 63, 1927–1938.
710 Reithmeier, H., Lazarev, V., Kubo, F., Rühn, W., Nolte, E., 2005. $^{129}$I in precipitation using a new
711 TOF system for AMS measurements, Nucl. Instrum. Methods Phys. Res. B 239, 273–280.
712 Reithmeier, H., Lazarev, V., Rühm, W., Nolte, E., 2010. Anthropogenic $^{129}$I in the atmosphere:
713 Overview over major sources, transport processes and deposition pattern, Sci. Total Environ.
714 408, 5052–5064.
715 Richardson, M. I., Toigo, A.D., and Newman, C.E., 2008. Planet WRF: A General Purpose, Local
716 to Global Numerical Model for Planetary Atmosphe re and Climate Dynamics, J. Geophys. Res.
717 112, E09001, doi:10.1029/2006JE002825.
718 Saiz‐Lopez, A., Plane, J.M.C., Baker, A.R., Carpenter, L.J., von Glasow, R., Martín, J.C.G.,
719 McFiggans, G. and Saunders, R.W., 2012a. Atmospheric chemistry of iodine., Chem. Rev. 112,
720 1773–804, doi:10.1021/cr200029u.
721 Santschi, P. H., Schink, D.R., Corapcioglu, O., Oktay‐Marshall, S., Fehn, U., and Sharma, P.,
722 1996. Evidence for elevated levels of iodine-129 in the Deep Western Boundary Current in the
723 Middle Atlantic Bight, Deep Sea Res. Part I, 43, 259–265, doi:10.1016/0967-0637(96)00005-2.

Schwehr, K. A., Santschi, P.H., and Elmore, D., 2005b. The dissolved organic iodine species of the isotopic ratio of $^{129}I/^{127}I$: A novel tool for tracing terrestrial organic carbon in the estuarine surface waters of Galveston Bay, Texas, Limnol. Oceanogr. Methods 3, 326–327.

Sellafield Ltd, 2016. Monitoring Our Environment, Discharges and Environmental Monitoring annual report 2015.

Skamarock, W.C., Klemp, J.B., Dudhia, J., Gill, D.O., Braker, D.M., Duda, M.G., Hung, X.-Y., Wang, W., Powers, J.G., 2008. A Description of the Advanced Research WRF Version 3. NCAR Technical Note.

Snyder. G., Aldahan, A., Possnert, G., 2010. Global distribution and long‐term fate of anthropogenic $^{129}I$ in marine and surface water reservoirs, Geochem. Geophys. Geosystems 11(4), doi:10.1029/2009GC002910.

Sportisse, B., 2007, A review of parameterizations for modelling dry deposition and scavenging of radionuclides, Atmos. Environ. 41, 2683–2698.

Stephens G.L., 1978 Radiation profiles in extended water clouds. 2: Parameterization schemes, J. Atmos. Sci. 35(11), 2133-2141.

Suzuki, T., Shoji, K., Amano, H., and Togawa, O., 2008. Measurement of iodine-129 in seawater samples collected from the Japan Sea area using accelerator mass spectrometry: Contribution of nuclear fuel reprocessing plants, Quat. Geochron. 3, 268–275, doi:10.1016/j.quageo.2007.12.004.

Tegtmeier, S., Krüger, K., Quack, B., Atlas, E., Blake, D.R., Boenisch, H., Engel, A., Hepach, H., Hossaini, R., Navarro, M.A., Raimund, S., Sala, S., Shi, Q., and Ziska, F., 2013. The contribution of oceanic methyl iodide to stratospheric iodine, Atmos. Chem. and Phys., 13, 11869–11886, doi.org/10.5194/acp-13-11869-2013.

Terada, M., Nagai, H., Yamazawa, H., 2013. Validation of a Lagrangian atmospheric dispersion model against middle-range scale measurements of $^{85}Kr$ concentration in Japan. J. Nucl. Sci. Technol. 50, 1198–1212.

Toyama, C., Muramatsu, Y. Igarashi, Y., Amoyama, M., Matsuzaki, H., 2013. Atmospheric Fallout of $^{129}I$ in Japan before the Fukushima Accident: Regional and Global Contributions (1963−2005), J. Environ. Radioact., 47, 8383–8390, dx.doi.org/10.1021/es401596z.

Toyama, C., Muramatsu, Y., Uchida, Y., Igarashi, Y., Amoyama, M., Matsuzaki, H., 2012. Variations of $^{129}I$ in the atmospheric fallout of Tokyo, Japan: 1963–2003, J. Environ. Radioact. 113, 116–122.

Tsukada H., Sanada, T., Ueno, T., Amano, H., 1995. Particulate and gaseous Cl, Br and I in the Chiba city atmosphere, Earozol Kenkyu 10(3), 214-220 (in Japanease).

Uematsu M., Merrill, J.T., Patterson, T.L., Duce, R.A. and Prospero, J.M., 1988. Aerosol residence time and iodine gas/particle conversion over the North Pacific as determined from Chernobyl radioactivity, Geochem. J. 22, 157-163.

Vogt, R., Fabian, P., Singh, O., 1999. The Handbook of Environmental Chemistry, vol. 4. Springer-Verlag.

763 Wagner, M.J.M., Dittich-Hannen, B., Synal, H.A., Suter, M., Schotterer, U., 1996. Increase of $^{129}I$
764 in the environment. Nucl. Instrum. Methods Phys. Res. Sect. B 259, 370–373.
765 Xu, S., Stewart, P.H.T., Hou, X., Watanabe, A., Yamaguchi, K. and Zhang, L., 2013. Iodine
766 Isotopes in Precipitation: Temporal Responses to $^{129}I$ Emissions from the Fukushima Nuclear
767 Accident, Environ. Sci. and Technol. 47, 10851-10859, dx.doi.org/10.1021/es401527q.
768 Yiou, F., Raisbeck, G.M., Zhou, Z.Q., and Kilius, L.R., 1994. $^{129}I$ from nuclear fuel reprocessing;
769 potential as an oceanographic tracer, Nucl. Instrum. Methods Phys. Res. Sect. B 92, 436–439,
770 doi:10.1016/0168-583X(94)96050-X.
771 Zhang, Y., Hemperly, J., Meskhidze, N., and Skamarock, W., 2012. The Global Weather Research
772 and Forecasting (GWRF) Model: Model Evaluation, Sensitivity Study, and Future Year
773 Simulation, Atmos. and Clim. Sci. 2(3), 231–253, doi: 10.4236/acs.2012.23024.
774 Zhang, L., Hou, X.L., Xu, S., 2016. Speciation of $^{127}I$ and $^{129}I$ in atmospheric aerosols at Risø,
775 Denmark: insight into sources of iodine isotopes and their species transformations, Atomos. Chem.
776 Phys. 16, 1971–1985, doi:10.5194/acpd-15-25139-2015.
777 Ziska, F., Quack, B., Abrahamsson, A., Archer, S.D., Atlas, E., Bell, T., Butler, J.H., Carpenter,
778 L.J., Jones, C.E., Harris, N.R.P., Hepach, H., Heumann, K.G., Hughes, C., Kuss, J., Kruger, K.,
779 Liss, P., Moore, R.M., Orlikowska, A., Raimund, S., Reeves, C.E., Reifenhauser, W.,
780 Robinson, A.D., Schall, C., Tanhua, T., Tegtmeier, S., Turner, S., Wang, L., Wallace, D.,
781 Williams, J., Yamamoto, H., Yvon-Lewis, S., and Yokouchi, Y., 2013. Global sea-to-air flux
782 climatology for bromoform, dibromomethane and methyl iodide, Atmos. Chem. Phys. 13, 8915–
783 8943, doi:10.5194/acp-13-8915-2013.

**Figure 1**

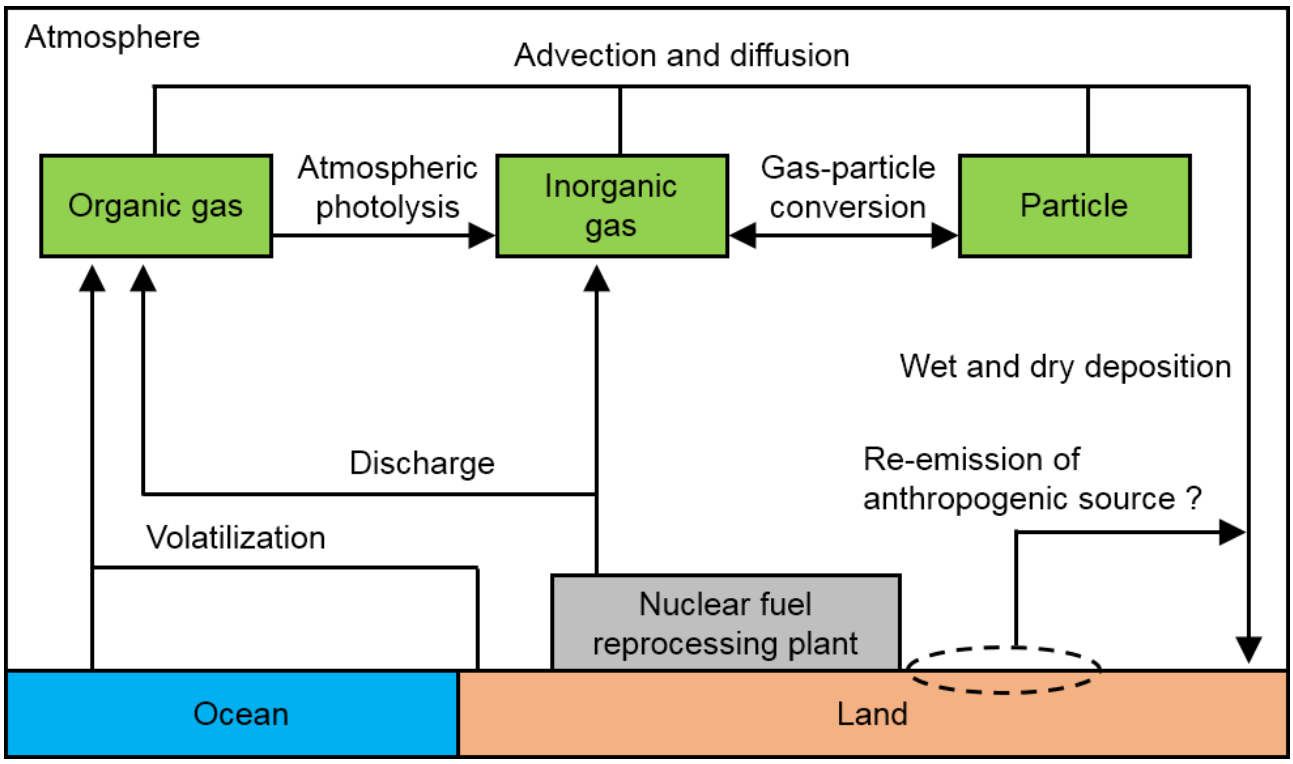


**Fig. 1**. Schematic illustration of known physical and chemical processes for global atmospheric $^{129}I$ cycle. The arrow of the re-emission of anthropogenic source near the nuclear fuel reprocessing plant is newly suggested in the present study.

**Figure 2**

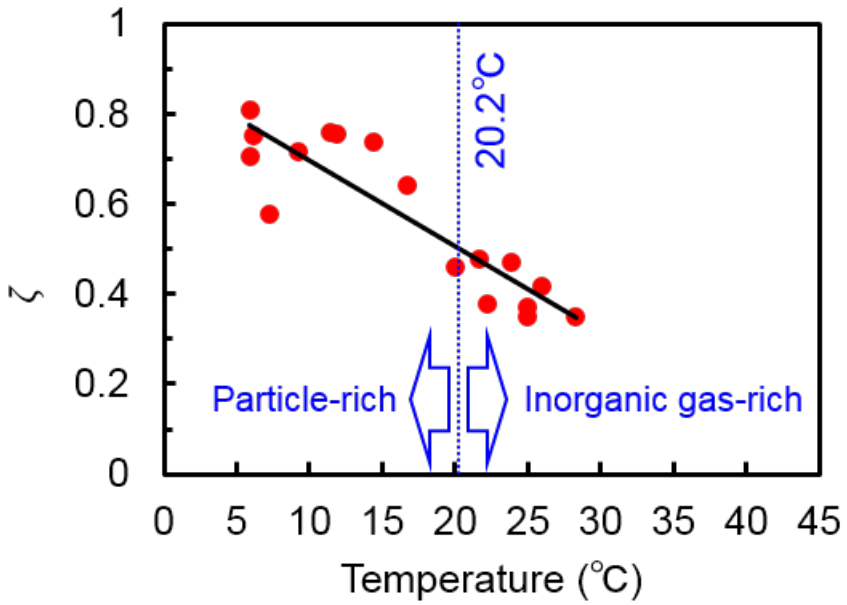


**Fig. 2**. Relationship between atmospheric temperature and $\zeta$ factor for the gas-particle conversion process. Red dots and the black line indicate measurements and the linear best fit based on the temperature and the factor, respectively. The correlation coefficient between atmospheric temperature and the factor is 0.803. When $\zeta = 0.5$, the temperature is approximately 20.2 °C.

**Figure 3**

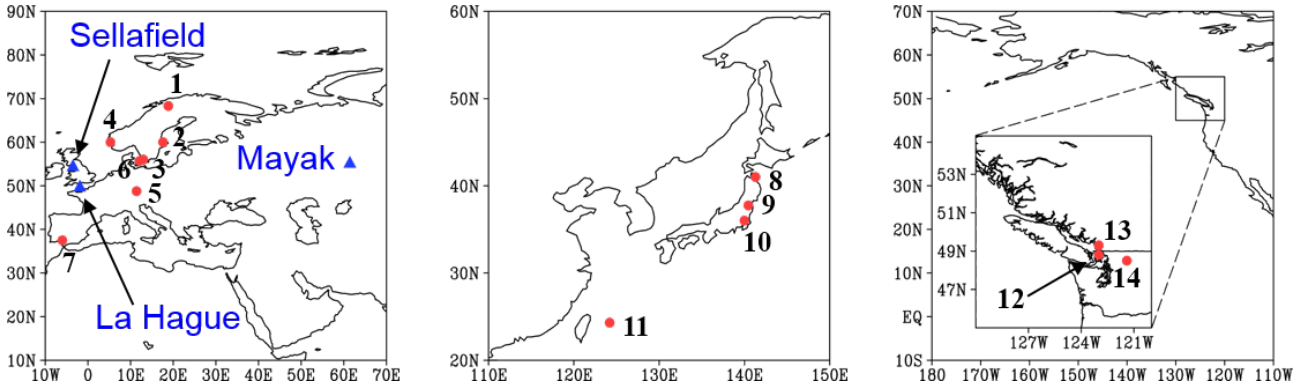


**Fig. 3**. Locations of nuclear fuel reprocessing plants (blue triangles) and measurement sites (red dots) in (a) Europe (1. Abisko, 2. Uppsala, 3. Kvidinge, 4. Bergen, 5. Bavaria, 6. Roskilde, 7. Seville), (b) Asia (8. Rokkasho, 9. Fukushima, 10. Tsukuba, 11. Ishigaki Island), and (c) North America (12. Vancouver, 13. Saturna Island, 14. NADP-WA19).

**Figure 4**

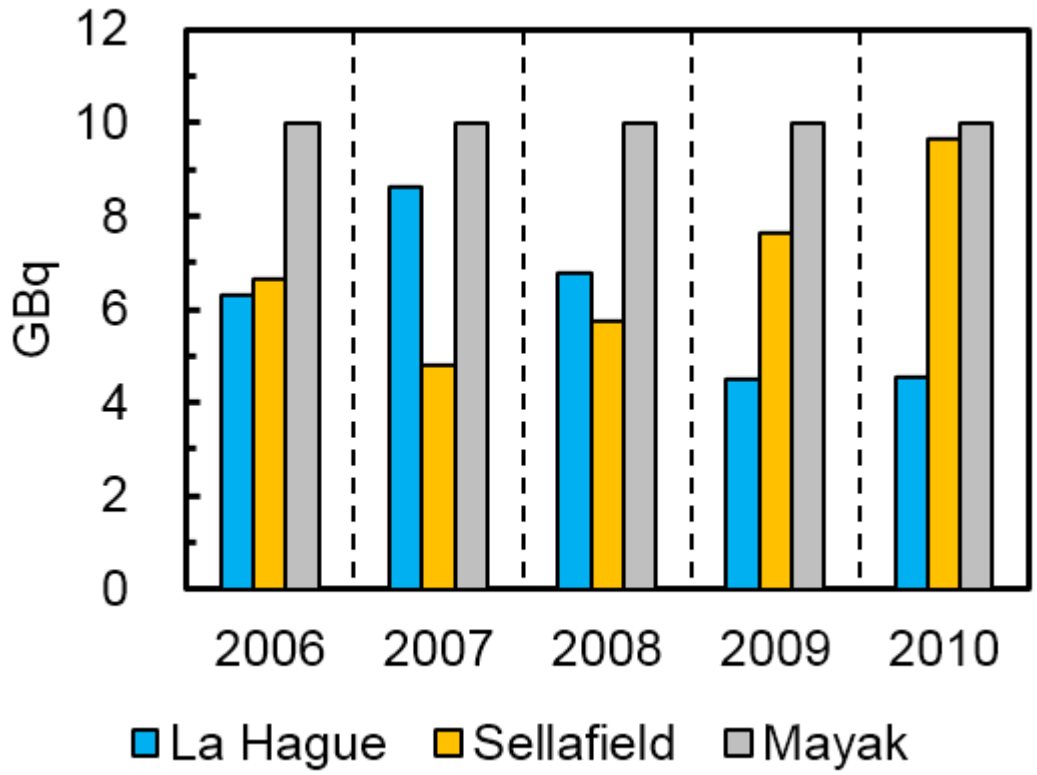


**Fig. 4**. Annual releases of gaseous $^{129}I$ from the nuclear fuel reprocessing plants at La Hague (light blue) and Sellafield (yellow), and estimates from Mayak (gray)

**Figure 5**

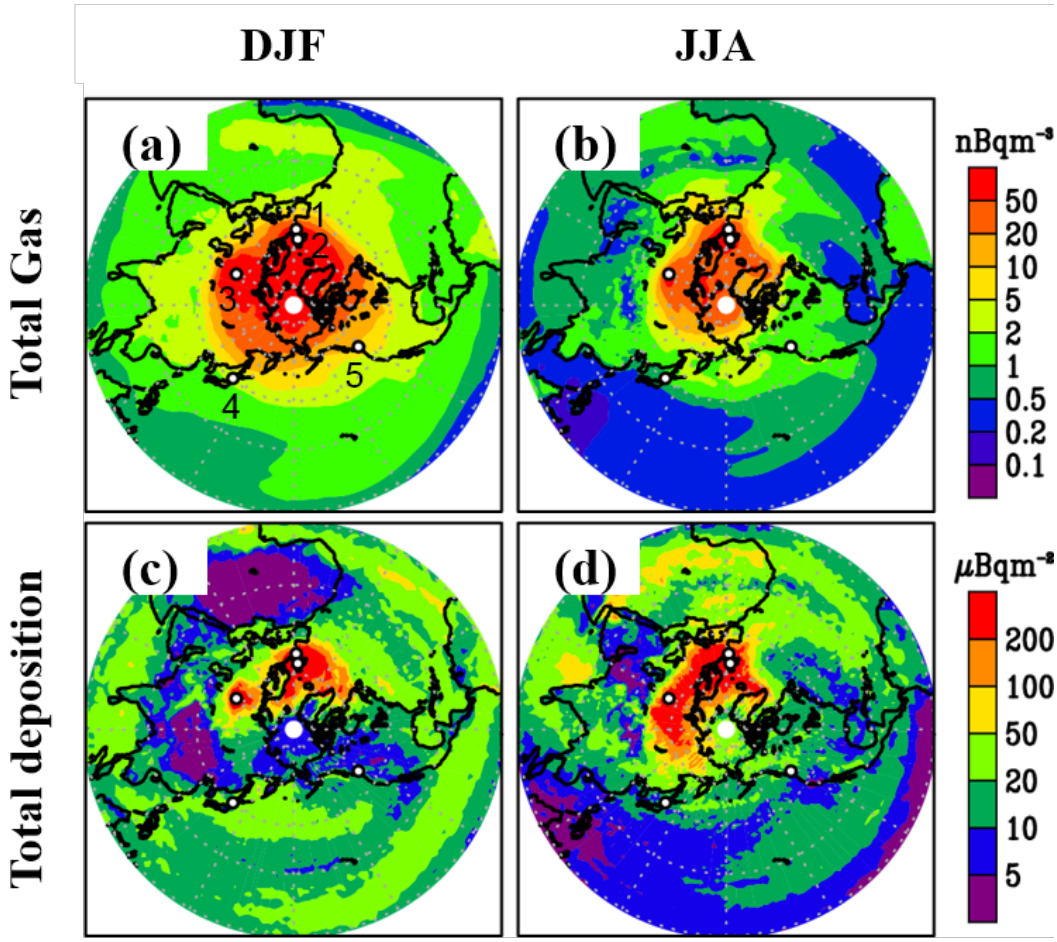


**Fig. 5.** Horizontal distribution of seasonally averaged (a-b) surface air concentration of total gaseous $^{129}I$ (nBq/m$^3$) and (c-d) accumulated total deposition of $^{129}I$ (μBq/m$^2$) from December 1, 2009, to February 28, 2010 (DJF), and from June 1 to August 31, 2010 (JJA), respectively, in the Control simulation. White dots show the sites of 1: La Hague, 2: Sellafield, 3: Mayak, 4: Rokkasho and 5: Vancouver.

**Figure 6**

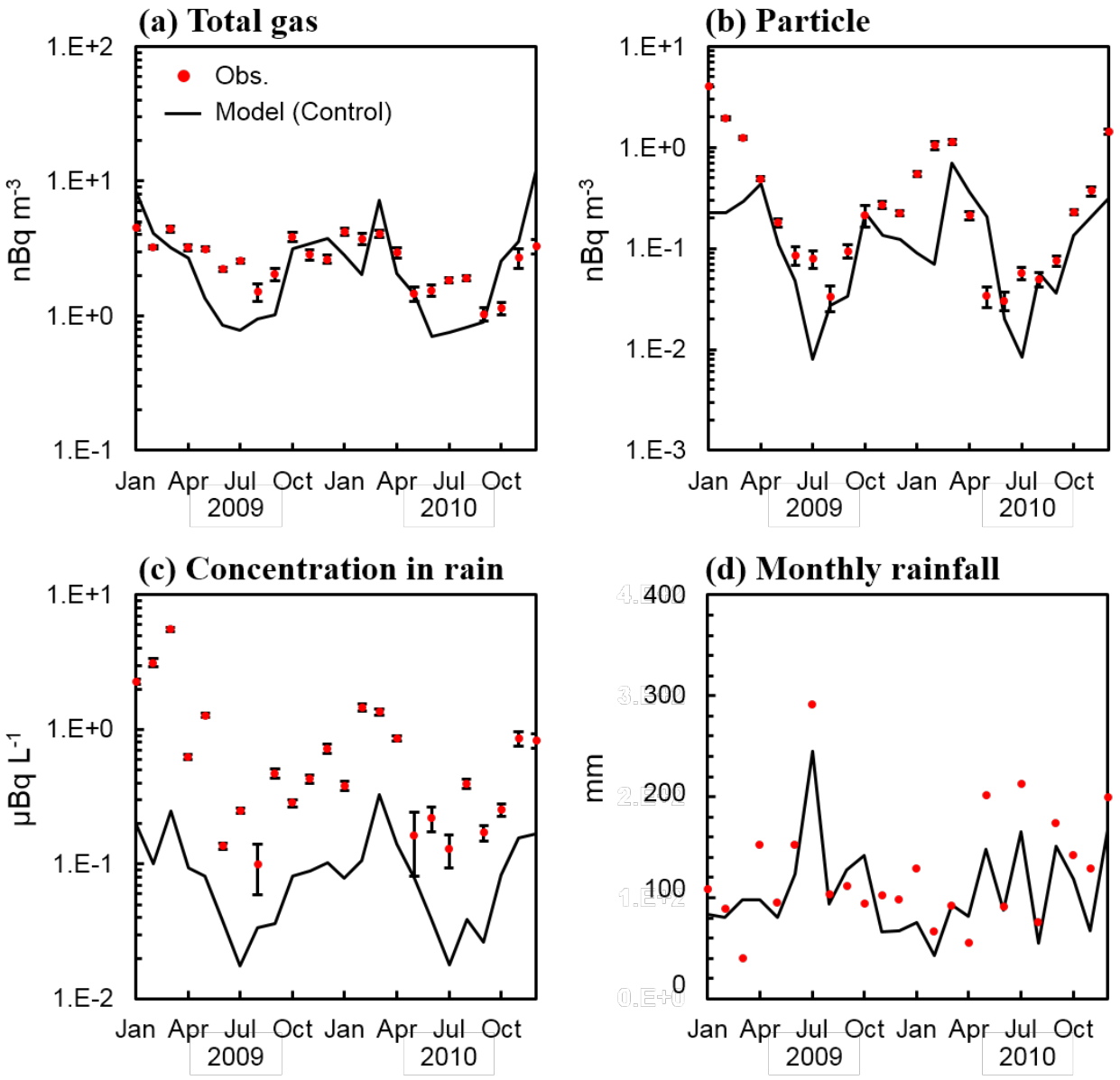


**Fig. 6**. Temporal variations of monthly values of Control-simulation (lines) and measurement (red dots) results for surface air concentration of (a) total gaseous and (b) particulate $^{129}I$ (nBq/m$^3$), (c) $^{129}I$ concentration in rain (μBq/L), and (d) monthly rainfall (mm) at Rokkasho.

**Figure 7**

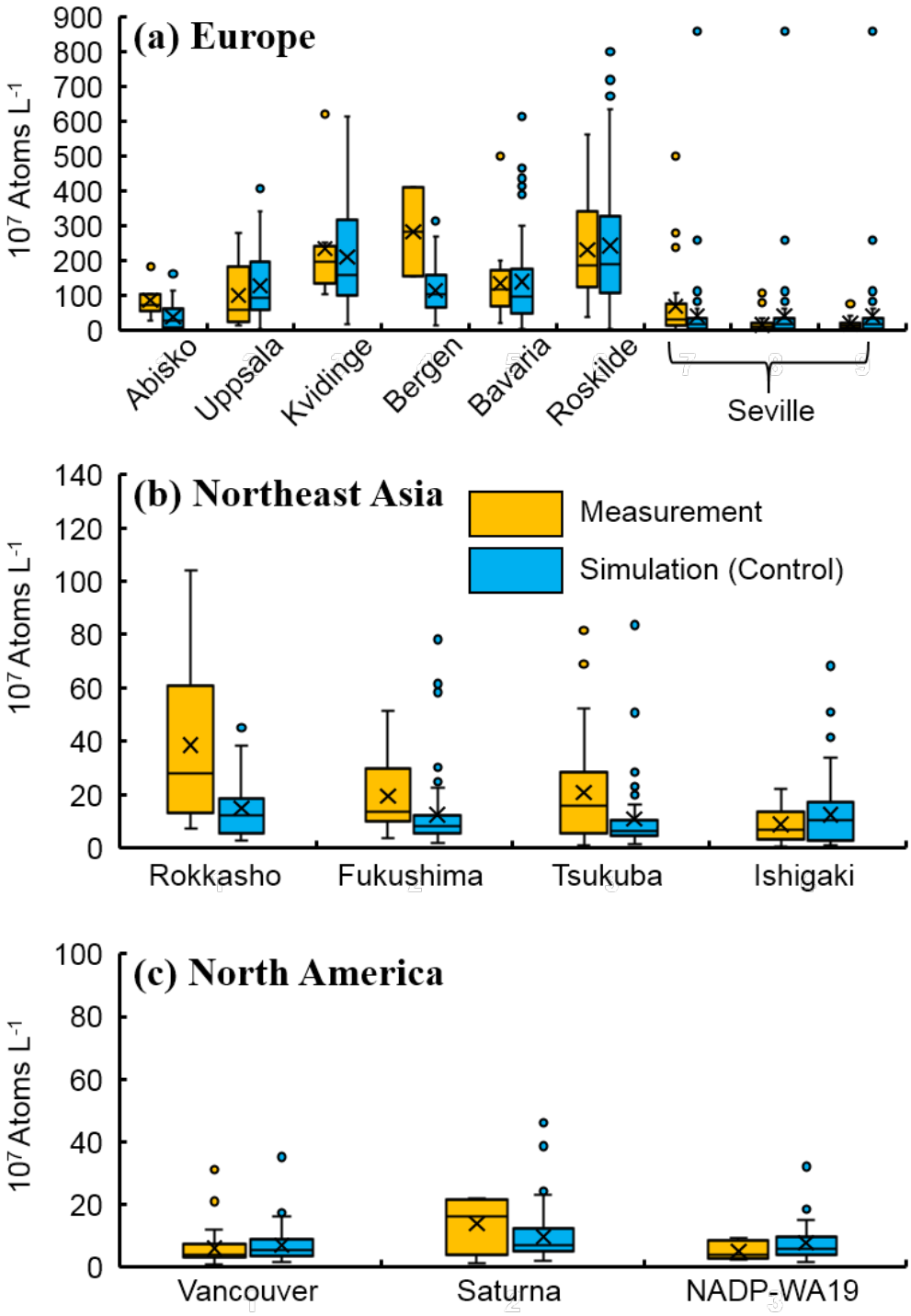


**Fig. 7**. Box and whisker plots of $^{129}$I concentration in rain (Atoms/L). Yellow and light blue boxes show the measured and simulated concentration, respectively. Mean values are indicated with cross-marks and median values with horizontal bars. The locations are shown and summarized in Fig. 3 and Table 4, respectively.

**Figure 8**

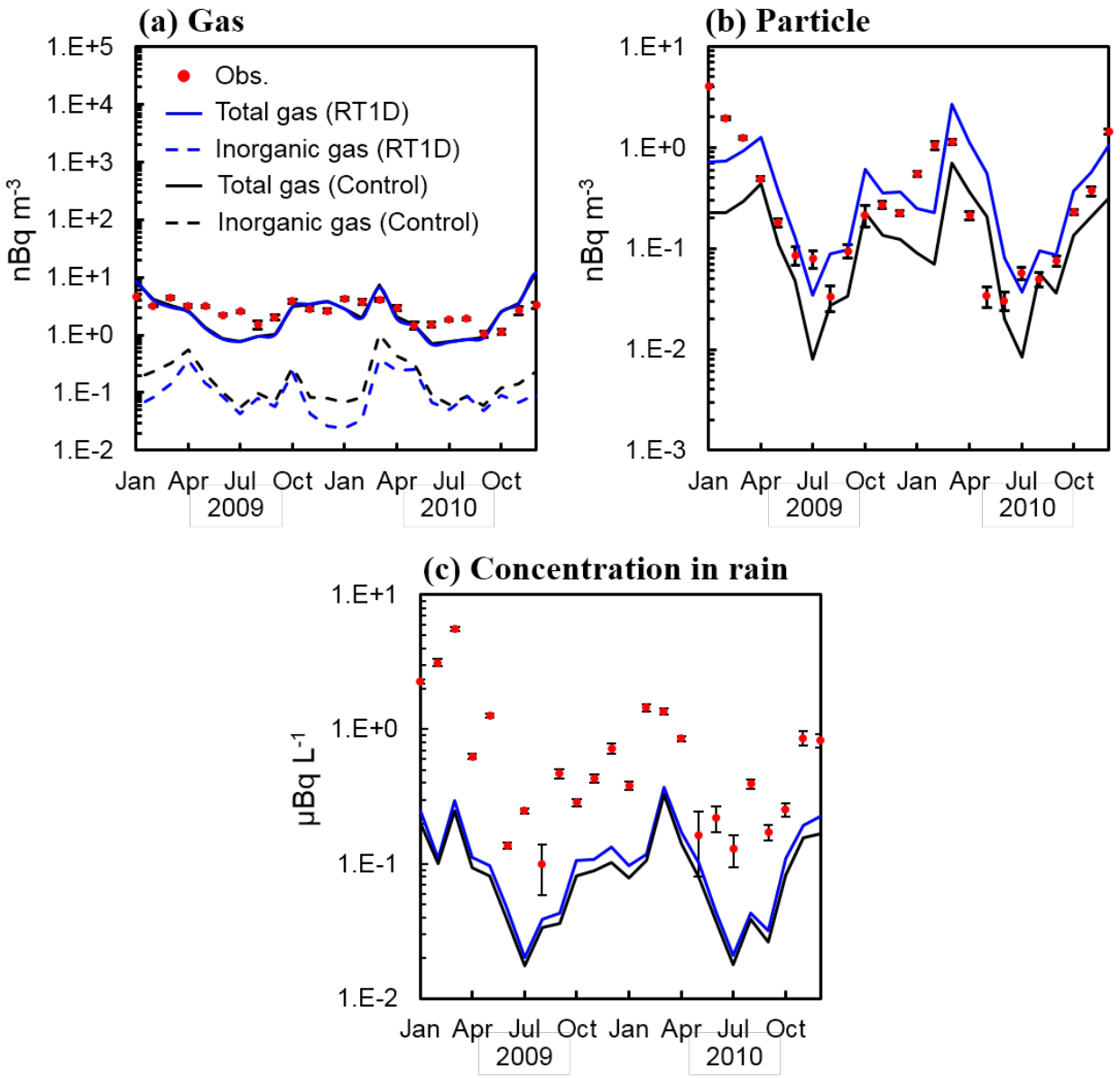


**Fig. 8**. Temporal variations of monthly values of simulation (lines) and measurement (red dots) result for surface air concentration of (a) gaseous and (b) particulate $^{129}I$ (nBq/m$^3$) and (c) $^{129}I$ concentration in rain (μBq/L) at Rokkasho. The black lines show the result of Control simulation and blue lines show that of RT1D one (1 day of the relaxation time) simulations, respectively. The total and inorganic gases are shown as solid and dashed lines in Fig. 8a, respectively. Note that the results of RT1D for gas mostly overlapped those of Control.

**Figure 9**

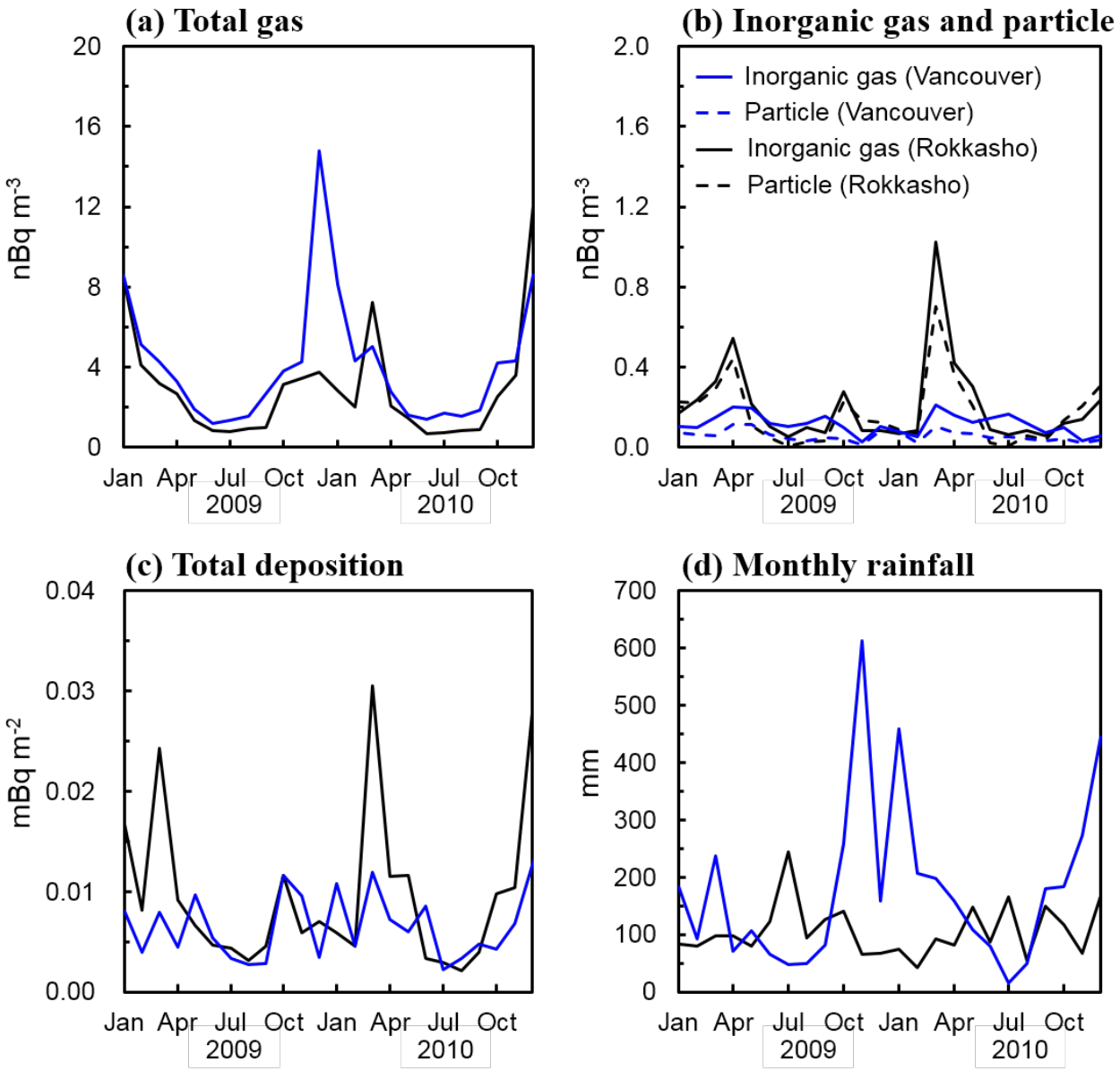


**Fig. 9.** Temporal variations of monthly values of Control-simulation result for (a) surface air concentration of total gaseous $^{129}I$ (nBq/m$^3$), (b) surface air concentration of inorganic gaseous and particulate $^{129}I$ (nBq/m$^3$), (c) total deposition of $^{129}I$ (mBq/m$^2$), and (d) monthly rainfall (mm) at Rokkasho (black line) and Vancouver (blue line) in the Control gas.

**Figure 10**

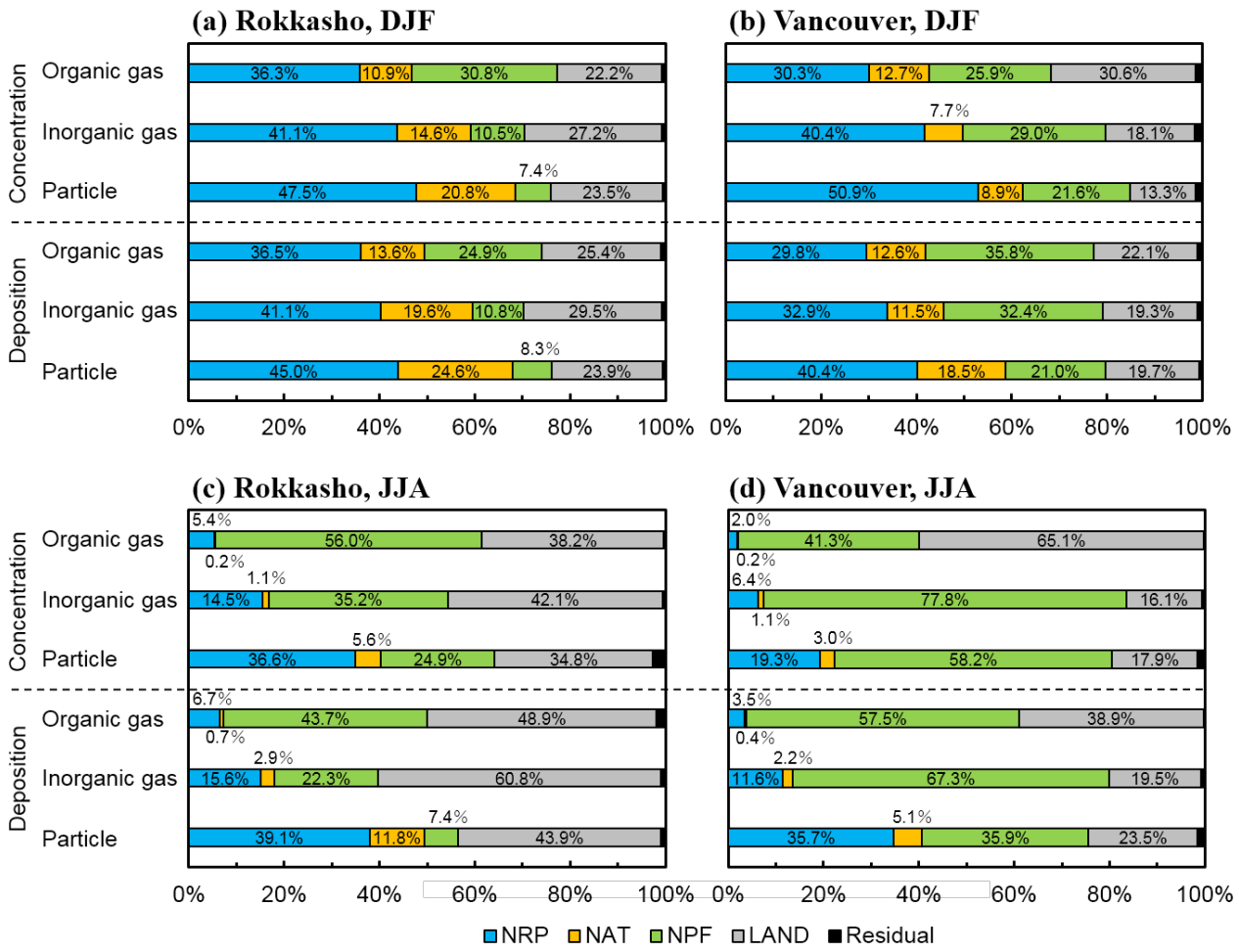


**Fig. 10.** Seasonal contribution rates (%) of source areas to surface air concentration of gaseous and particulate $^{129}I$ and deposition of $^{129}I$ at Rokkasho and Vancouver. The value of contribution rate is calculated by dividing concentration (or deposition) of sensitivity simulation by concentration (or deposition) of Control simulation. The simulation scenarios of NRP ($^{129}I$ emission from nuclear fuel reprocessing plants), NAT ($^{129}I$ emission from the North Atlantic Ocean), NPF ($^{129}I$ emission from the North Pacific Ocean) and LAND ($^{129}I$ emission from land surface) are summarized in Table. 1.The contribution rate in DJF and JJA are calculated using monthly averaged values in December, January and February in 2009 and 2010, and those in June, July and August in 2009 and 2010, respectively.

**Figure 11**

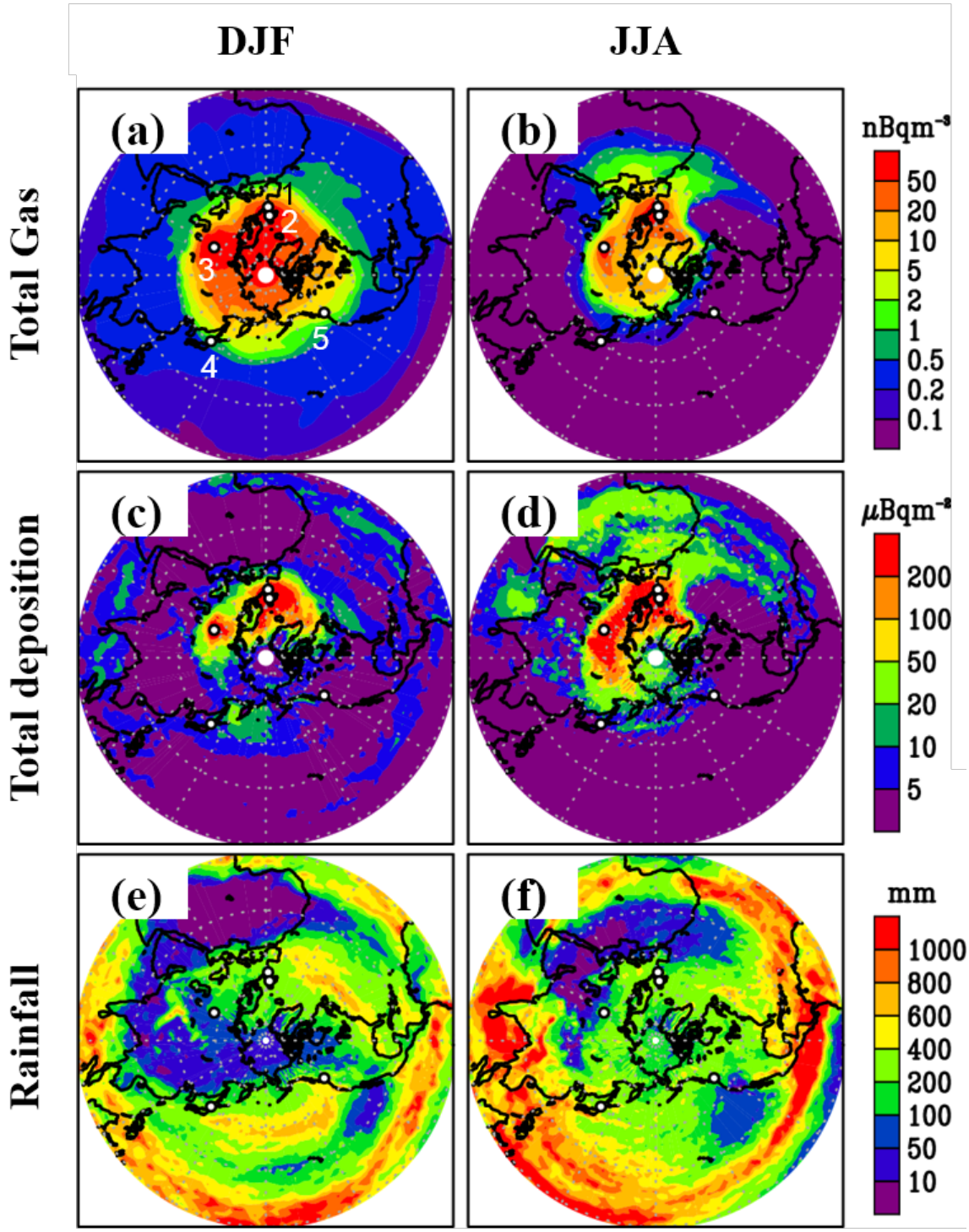


**Fig. 11.** Horizontal distribution of seasonally averaged (a-b) surface air concentration of total gaseous $^{129}I$, (c-d) accumulated total deposition of $^{129}I$ and (e-f) accumulated rainfall from December 1, 2009, to February 28, 2010 (DJF), and from June 1 to August 31, 2010 (JJA), respectively, in the NRP ($^{129}I$ emission from nuclear fuel reprocessing plants) simulation. White dots show the sites of 1: La Hague, 2: Sellafield, 3: Mayak, 4: Rokkasho and 5: Vancouver.

884 **Figure A1**

885

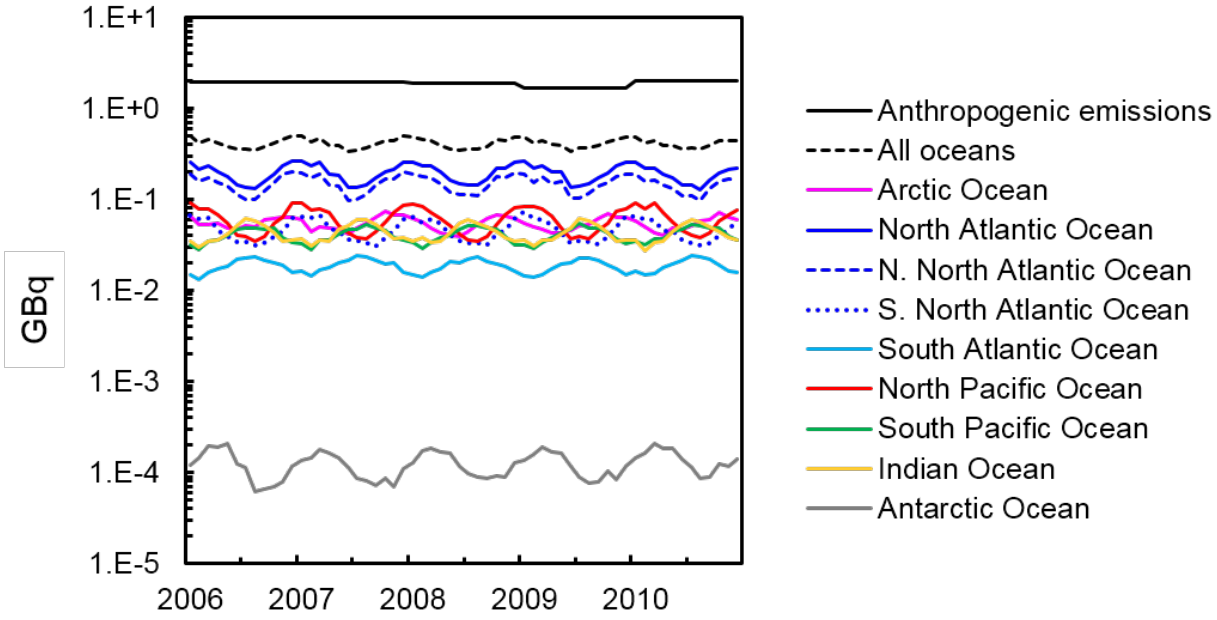


886

887

888 **Fig. A1.** Temporal variations of monthly volatilization fluxes of $^{129}I$ from ocean calculated in our
889 model. Anthropogenic emission is additionally shown as solid black line. All oceans (dashed black
890 line) and North Atlantic Ocean (solid blue line) indicate the sum of volatilization flux of $^{129}I$ from
891 total oceans, and the sum of volatilization flux of $^{129}I$ from northern and southern areas of the North
892 Atlantic Ocean, respectively.

**Table 1.** Settings for the WRF and atmospheric iodine-129 transport models. For the NRP simulation, we set the $^{129}I$ volatilization fluxes of ocean and land to zero. On the other hand, for the NAT and NPF simulations, we set the flux of $^{129}I$ other than from the North Atlantic Ocean and the North Pacific Ocean, respectively, to zero. For the LAND simulation, we set the anthropogenic release from the nuclear fuel reprocessing plants and $^{129}I$ volatilization fluxes of ocean, respectively, to zero. Additionally, the RT1D simulation, in which 1 day of the relaxation time was used, were conducted.

| | WRF | atmospheric iodine-129 transport model | | | | | |
|---|---|---|---|---|---|---|---|
| | | Control | NRP | NAT | NPF | LAND | RT1D |
| Number of horizontal grid | | | | 257 × 129 | | | |
| Time step | | | | 600 s | | | |
| Vertical levels | 28[a] | | | | 25 | | |
| Boundary and initial conditions | ERA-interim[b] | - | - | - | - | - | - |
| Anthropogenic emission | | La Hague, Sellafield and Mayak | La Hague, Sellafield and Mayak | No | No | No | La Hague, Sellafield and Mayak |
| Natural emission | - | All oceans[c] and land[d] | No | North Atlantic Ocean[c] | North Pacific Ocean[c] | Land[d] | All oceans[c] and land[d] |
| Relaxation time | | 14 days | 14 days | 14 days | 14 days | 14 days | 1 day |

[a] Eta levels from the surface to 100 hPa: 1.00, 0.99, 0.978, 0.964, 0.946, 0.922, 0.894, 0.86, 0.817, 0.766, 0.707, 0.644, 0.576, 0.507, 0.444, 0.38, 0.324, 0.273, 0.228, 0.188, 0.152, 0.121, 0.093, 0.069, 0.048, 0.029, 0.014, and 0.00.

[b] ECMWF global atmospheric reanalysis (horizontal resolution: approximately 80 km).

[c] Except for sea ice areas.

[d] Except for desart areas.

**Table 2.** Area-averaged $^{129}I/^{127}I$ ratios used to calculate $^{129}I$ volatilization flux from ocean surfaces.

| Area | $^{129}I/^{127}I$ ratio | Reference |
|---|---|---|
| Arctic Ocean | $8.5 \times 10^{-9}$ | Yuio et al. (1994), Hou (2004) and Hou et al. (2007) |
| North Atlantic Ocean[a] | | |
| Northern area | $2.1 \times 10^{-9}$ | Yiou et al. (1994), Edmonds et at. (1998) and Hou (2004) |
| Southern area | $1.7 \times 10^{-10}$ | Santschi et al. (1996) and Schwehr et al. (2005b) |
| South Atlantic Ocean | $5.0 \times 10^{-11}$ | Snyder et al. (2010) |
| North Pacific Ocean | $1.6 \times 10^{-10}$ | Li et al. (2005), Nies et al. (2009), and Suzuki et al. (2008) |
| South Pacific Ocean | $5.0 \times 10^{-11}$ | Snyder et al. (2010) |
| Indian Ocean | $2.4 \times 10^{-10}$ | Nies et al. (2009) |
| Antarctic Ocean | $1.5 \times 10^{-12}$ | Snyder et al. (2010) |

[a] The boundary between northern and southern areas is 50°N.

**Table 3.** Statistical analysis between measured and simulated monthly surface air concentrations (nBq/m$^3$), monthly rainfall (mm), and monthly total deposition (concentrations in rain) (μBq/L) at Rokkasho. The values of SD, MB, RMSE and R show standard deviation of the simulation and measurement, the mean bias, root mean square error, and correlation coefficient, respectively.

| | Mean (nBq/m$^3$) | | Min. / Max (nBq/m$^3$). | | Median (nBq/m$^3$) | | SD (nBq/m$^3$) | | | | | | |
|---|---|---|---|---|---|---|---|---|---|---|---|---|---|
| | Obs. | Model | Obs. | Model | Obs. | Model | Obs. | Model | MB (nBq/m$^3$) | RMSE (nBq/m$^3$) | R | RSMM[a] | FA2[b] |
| Total gas | 2.75 | 2.95 | 1.03 / 4.52 | 0.70 / 12.0 | 2.77 | 2.29 | 1.03 | 2.71 | 0.20 | 2.31 | 0.56 | 0.83 | 0.63 |
| Particle | 0.59 | 0.17 | 0.03 / 4.05 | 0.01 / 0.70 | 0.22 | 0.13 | 0.89 | 0.16 | -0.42 | 0.94 | 0.36 | 0.59 | 0.54 |
| Total depo. | 0.93 | 0.10 | 0.10 / 5.57 | 0.02 / 0.33 | 0.45 | 0.08 | 1.21 | 0.07 | -0.83 | 1.43 | 0.62 | 0.18 | 0.04 |
| Rainfall | 125.4 | 106.6 | 40.5 / 291.5 | 43.0 / 244.9 | 106.3 | 93.5 | 56.5 | 44.6 | -18.8 | 39.3 | 0.84 | 0.87 | 0.96 |

[a] Ratio of simulated-to-measured medians.

[b] Fraction of data within factors of 2.

912 **Table 4.** Description of observational sites in Fig. 7.

| No. [a] | Site, country | Years for measurement | Concentration ($10^7$ atoms $L^{-1}$) | Number of data | Reference |
|---|---|---|---|---|---|
| Europe | | | | | |
| 1 | Abisko, Sweden | 2000–2001 | 29–184 | 7 | Persson et al. (2007) |
| 2 | Uppsala, Sweden | 1999–2002 | 17–282 | 14 | Persson et al. (2007) |
| 3 | Kividinge, Sweden | 2001–2002 | 104–623 | 8 | Persson et al. (2007) |
| 4 | Bergen, Norway | 2003 | 158–410 | 2 | Persson et al. (2007) |
| 5 | Bavaria, Germany | 2003–2004 | 21–500 | 16 | Reithmeier et al. (2005) |
| 6 | Roskilde, Denmark | 2001–2006 | 50.9–563.3 | 70 | Xu et al. (2013) |
| 7 | Seville, Spain | 1996–1997 | 4.7–500 | 35 | López-Gutiérrez et al. (2001) |
| 7 | Seville, Spain | 1998–1999 | 2.2–107.8 | 32 | López-Gutiérrez et al. (2004) |
| 7 | Seville, Spain | 2005–2008 | 2.6–88.6 | 38 | Gómez-Guzmán et al. (2012b) |
| Asia | | | | | |
| 9 | Fukushima, Japan | 2011–2012 [b] | 3.6–51.3 | 14 | Xu et al. (2013) |
| 10 | Tsukuba, Japan | 1986–2005 | 1–82 | 36 | Toyama et al. (2013) |
| 11 | Ishigaki Island, Japan | 1979–2003 | 2.2–21.9 | 23 | Toyama et al. (2013) |
| North America | | | | | |
| 12 | Vancouver, Canada | 2011–2012 | 10.87–310.74 | 38 | Herod et al. (2015) |
| 13 | Satura Island, USA | 2011–2012 | 13.19–220.65 | 7 | Herod et al. (2015) |
| 14 | NADP-WA19, USA | 2011–2012 | 25.77–95.42 | 4 | Herod et al. (2015) |

913 [a] Indicated numbers in Fig. 3.

914 [b] Period from March to December 2011 is not included to avoid the feefect of the Fukushima Dai-ichi Nuclear Power Station accident.